JOURNAL OF GEOPHYSICAL RESEARCH, VOL. 100, NO. B4, PAGES 6097–6120, APRIL 10, 1995

Crustal fissuring and its relationship to magmatic and hydrothermal processes on the East Pacific Rise crest (9°12' to 54'N)

Dawn J. Wright[1]
Departments of Geography and Geological Sciences, University of California, Santa Barbara

Rachel M. Haymon
Department of Geological Sciences and Marine Science Institute, University of California, Santa Barbara

Daniel J. Fornari[2]
Department of Geology and Geophysics, Woods Hole Oceanographic Institution, Woods Hole, Massachusetts

Abstract. The deep-towed *Argo I* optical/acoustical vehicle and a geographic information system (GIS) have been used to establish the abundance, widths, and spatial distribution of fissures, as well as the relative age distribution of lavas along the narrow (<500 m wide) axial zone of the East Pacific Rise (EPR) from 9°12' to 9°54'N. On a second-order scale (~78 km long), wider but less numerous fissures are found in the northern portion of the survey area; this changes to narrower, more abundant fissures in the south. A profile of the cumulative width added by fissures to the axial zone exhibits minima in three areas along strike (near 9°49', 9°35', and 9°15'N), where the most recent eruptions have occurred above sites of magmatic injection from the upper mantle, filling and covering older fissures. On a fourth-order scale (5-15 km long) the mean density of fissuring on a given segment is greater where relative axial lava age is greater. Fissure density also correlates with hydrothermal vent abundance and type. Increased cracking toward segment tips is observed at the second-order scale, whereas fourth-order segments tend to be more cracked in the middle. Cracking on a fourth-order scale may be driven by the propagation of dikes, rather than by the far-field plate stresses. The above relations constrain the model of *Haymon et al.* [1991] in which individual fourth-order segments are in different phases of a volcanic-hydrothermal-tectonic cycle.

Introduction

Recent mapping of the global mid-ocean ridge system (MOR) with high-resolution sonar systems has shown that the morphology of spreading centers is far from uniform, displaying variation in both space and time [e.g., *Macdonald et al.*, 1984, 1988a, 1991, and references therein; *Lonsdale*, 1985, 1989; *Grindlay et al.*, 1992]. A prevalent interpretation of these observations, in conjunction with relevant petrologic and seismic data [e.g., *Langmuir et al.*, 1986; *Detrick et al.*, 1987; *Sinton and Detrick*, 1992], is that variations in magma supply along the MOR partition the ridge along strike into a hierarchy of distinct accretionary segments bounded by various types and orders of ridge-axis discontinuities. These discrete ridge segments represent the fundamental "building blocks" of the global MOR system. *Macdonald et al.* [1991] summarized the hierarchy of ridge segments as follows: first-order segments are tectonically bounded by major transform faults and propagating rifts at length intervals of 300-500 km; second order segments, typically 50-300 km long, are bounded by large-offset (>3-5 km) overlapping spreading centers (OSCs) at intermediate- to fast-spreading centers, and small-offset, nonrigid transform faults at slow-spreading centers; third-order segments, 30-100 km long, are bounded by small-offset (0.5-2 km) OSCs at intermediate- to fast-spreading centers; fourth-order segments, 10-50 km long, are bounded by very small lateral offsets of linear axial features (such as summit calderas, grabens, horsts, pillow ridges), or by small bends (1°-5°) in the ridge axis (deviations in axial linearity or "devals" [*Langmuir et al.*, 1986]).

The character and evolution of individual MOR segments is not well known. In particular, the spatial and temporal stability of segments in different spreading regimes and in various stages of volcanic, hydrothermal, and tectonic activity needs to be determined. This includes the sequence, evolution, and interaction of tectonic, magmatic, and hydrothermal processes within individual segments as well as the dynamic interaction at boundaries between these segments. Because fissures provide essential pathways into the upper oceanic crust through which magma and hydrothermal fluids can migrate, the nature and distribution of

[1]Now at NOAA-PMEL, Hatfield Marine Science Center, Newport, Oregon.

[2]Formerly at Lamont-Doherty Earth Observatory, Columbia University, Palisades, New York.

Paper number 94JB02876.
0148-0227/95/94JB-02876$05.00

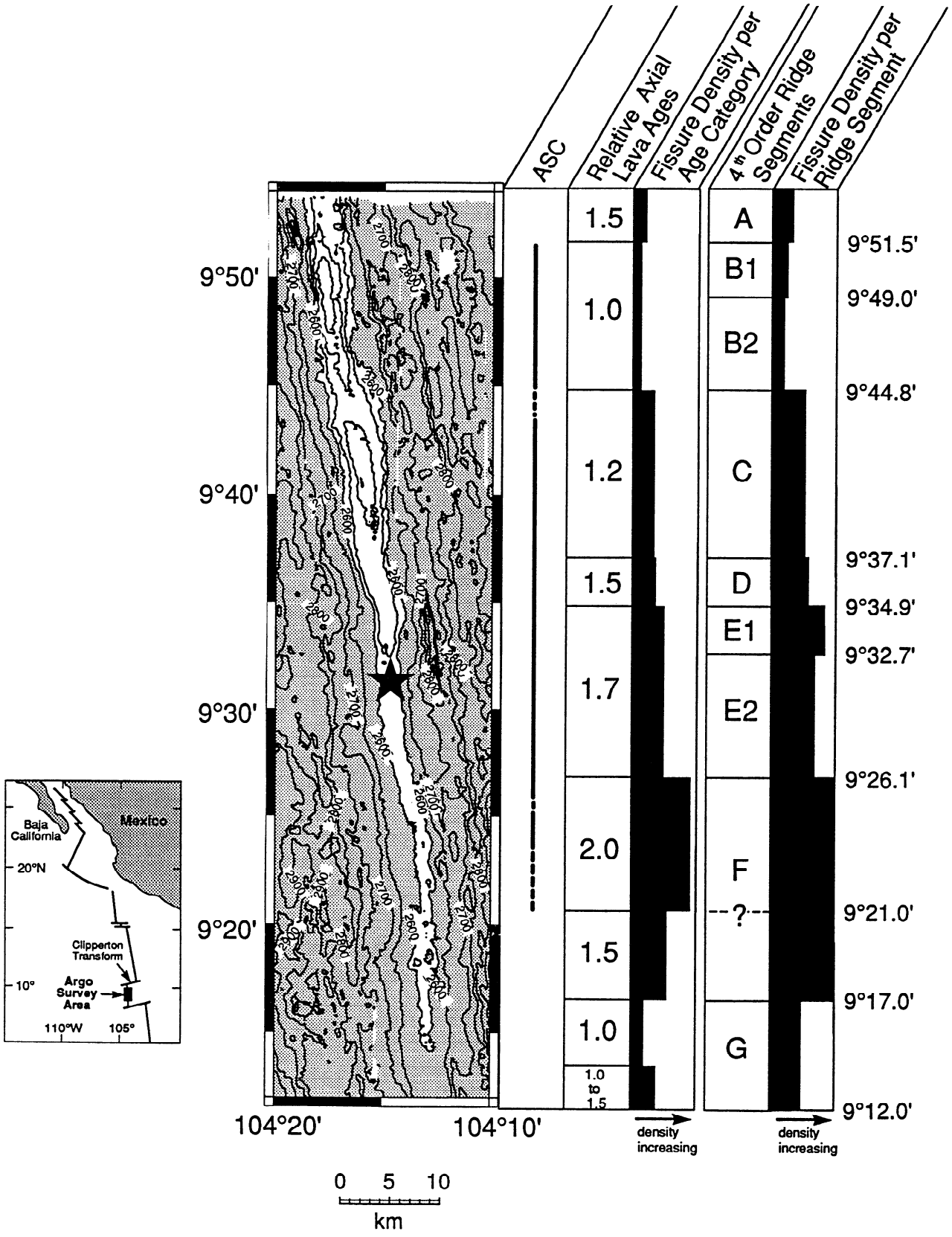
ASC
Relative Axial Lava Ages
Fissure Density per Age Category
4th Order Ridge Segments
Fissure Density per Ridge Segment
9°50'
9°40'
9°30'
9°20'
104°20'
104°10'
1.5
1.0
1.2
1.5
1.7
2.0
1.5
1.0
1.0 to 1.5
A
B1
B2
C
D
E1
E2
F
?
G
9°51.5'
9°49.0'
9°44.8'
9°37.1'
9°34.9'
9°32.7'
9°26.1'
9°21.0'
9°17.0'
9°12.0'
density increasing
density increasing
Mexico
Baja California
20°N
10°
Clipperton Transform
Argo Survey Area
110°W
105°
0 5 10
km

fissuring provide some clues to the behavior of segments and have important implications for magmatic and hydrothermal venting along the MOR crest. The nature and distribution of fissuring are the primary topics of this study.

Several previous studies have included detailed mapping of the distribution and orientation of fissures on MOR crests spreading at different rates [e.g., *Normark*, 1976; *Luyendyk and Macdonald*, 1977; *Gente et al.*, 1986; *Kappel and Ryan*, 1986; *Crane*, 1987; *Chadwick et al.*, 1991; *Edwards et al.*, 1991; *Embley et al.*, 1991]. *Crane* [1987] also considered the implications of fissure density and length in the neovolcanic zone. These studies agree on the following spatial and temporal aspects of fissure distribution: (1) most fissuring occurs primarily on the crest of the MOR in a 1- to 2-km-wide region within the neovolcanic zone; (2) lengths and widths of fissures are generally 10-500 and 0.2-3 m respectively; (3) orientations are largely subparallel to the adjacent ridge axis; and, (4) spacings are usually <100 m. Most workers agree that the presence of fissures is due to either (a) magmatic intrusion (extensional cracking in the crust overlying magmatic diapirs or dikes), (b) lithospheric stretching (amagmatic, tensile cracking as the ridge accelerates from zero velocity to its full spreading rate), or (c) thermal contraction of aging crust. Where the ridge has recently erupted, axial fissures formed by these mechanisms may be filled or covered by new, uncracked lava flows. Such contact relationships have been commonly observed in areas where very recent eruptions have been documented such as at the EPR, 9°45'-51'N [*Haymon et al.*, 1993], and at the CoAxial site on the Juan de Fuca Ridge [*Embley et al.*, 1993].

Detailed discussion of the mechanics of fissure formation have been presented in studies of the subaerial structure of Iceland, Hawaii, and Afar, where quantitative field measurements and resulting theoretical models have allowed for a more thorough treatment of the problem [e.g., *Pollard et al.*, 1983; *Rubin and Pollard*, 1987, 1988; and *Gudmundsson and Bäckström*, 1991]. These results are directly applicable to the MOR environment because the same mechanical processes are at work. Fissure formation in Iceland, Hawaii, and Afar has been attributed mainly to tensile stresses generated either by dike intrusions or by divergent plate motion. Dike emplacement produces significant changes in the local stress field of crustal rock directly over the top of the dike. In the dike model developed by *Pollard et al.* [1983], contours of maximum principal stress outline a region of tensile stress that spreads outward and upward from the top of the dike. The point immediately over the dike at the surface is stress free and a pair of tensile maxima occurs on either sides of this spot. In contrast with this dike model, a simple plate motion model assumes that tensile stress due to far-field stresses builds up gradually within the rift zone until new fissures form, old ones propagate, and tensile stress is temporarily relaxed [*Björnsson*, 1985].

In this study the high-resolution, near-bottom imaging capability of the *Argo I* optical/acoustical system [*Harris and Ballard*, 1986] has been used to establish the abundance, widths, and spatial distribution of fissures, as well as the inferred relative age distribution of lavas, along the axial zone of the fast-spreading East Pacific Rise (EPR) between 9°12'N and 9°54'N (full spreading rate is equal to 11 cm/yr; [*Klitgord and Mammerickx*, 1982]). *Argo I* video and sonar data were used to create distribution maps for most of the second-order ridge segment between the Clipperton transform and the 9°03'N OSC, including nine fourth-order segments. Statistical analyses characterize fissure density, width, and length on both a second- and a fourth-order segment scale. The results were used to test and further develop the model of cyclic volcanic-hydrothermal-tectonic activity postulated by *Haymon et al.* [1991]. Volcanic-tectonic cycles have been proposed in numerous previous studies of the EPR [e.g., *Gente et al.*, 1986; *Crane et al.*, 1988; *Haymon et al.*, 1991], the Mid-Atlantic Ridge [e.g., *Crane and Ballard*, 1981; *Eberhart et al.*, 1988; *Fouquet et al.*, 1993], the Juan de Fuca Ridge [e.g., *Lichtman and Eissen*, 1983; *Embley et al.*, 1991], and the Galapagos Rift [e.g., *Embley et al.*, 1988]. The present study is one of the first efforts to quantitatively investigate MOR volcanic-tectonic cycles and hydrothermal activity at the spatial scale of a whole ridge segment using data that are sufficiently dense, continuous, and geographically precise for meaningful analysis by statistical methods.

Figure 1. Distribution of tectonic and volcanic features along the East Pacific Rise (EPR)crest from 9°12' to 9°54'N, modified from *Haymon et al.* [1991]. Inset map shows the location of the *Argo I* survey area on the northern EPR. Sea Beam bathymetry to the left of the inset map is from the data of *Wilcock et al.* [1993]. Contour interval is 50 m except for regions shallower than 2600 m where the contour interval is 20 m. Star shows the location of Ocean Drilling Program (ODP) Hole 864A. Moving to the right, the columns show the distribution of various features along strike. Note that axial lava age and fissure density generally increase from segment B1 in the north through segment F in the south. Note also the excellent correlation between older relative lava ages and increased fissure abundance along individual fourth-order segments. The delineation of the axial summit caldera (ASC) in the left column is based on the combined analysis of *Argo I* video and sonar data (Figure 2 and D. J. Fornari et al., unpublished data, 1993) and SeaMARC II sonar data [*Macdonald et al.*, 1992]. The ASC is well developed (wall bounded) in the regions denoted by a solid line. The dashed portions of the line denote sections of the ridge axis where the ASC is poorly developed, i.e., where the axial zone exhibits extensive fissuring and/or collapse that is not scarp bounded on both sides. The next two columns to the right show the inferred relative axial ages of lavas along strike and the density of fissures per lava age category. Density refers to fissure abundance (or number) per square kilometer of seafloor imaged within a particular lava age category. Relative ages are inferred from criteria given in Table 1 of *Haymon et al.* [1991] and averaged within each ridge segment (see text). The two columns to the right show the locations of "deval"-bounded, fourth-order ridge segments as determined by *Haymon et al.* [1991] and the fissure density per ridge segment (i.e., abundance (or number) of fissures per square kilometer of seafloor imaged within a particular segment).

Data Acquisition

In late 1989 the *Argo I* seafloor imaging system was used to conduct a near-bottom survey of the narrow (<500 m wide) axial zone of the East Pacific Rise (EPR) between 9°09'N and 9°54'N (Figure 1) [*Haymon et al.*, 1991]. Developed, owned, and operated by the Deep Submergence Laboratory of the Woods Hole Oceanographic Institution, *Argo I* consists of a deep-towed, negatively buoyant towfish deployed on standard 1.73-cm (0.680 in.) coaxial armored cable [*Harris and Ballard*, 1986; *Gallo et al.*, 1990]. *Haymon et al.* [1991] describe the logistics and the configuration of *Argo I* for the survey.

During the 21-day survey of the EPR crest, *Argo I* provided dense data coverage along multiple, closely spaced (10-50 m) tracklines (Figure 2) along ~80 km of the EPR crest. The 100-kHz, side-looking sonar (300-m full swath) provided 90% coverage within an 800-m-wide swath of terrain centered on the EPR axis [*Fornari et al.*, 1990; *Haymon et al.*, 1991; D. J. Fornari et al., unpublished data, 1993]. The sonar data were used to delineate the boundaries of a linear axial summit caldera (ASC), <300 m wide and ~8 to ≤15 m deep. This feature is thought to be formed principally through volcanic collapse within the axial zone between 9°51.5'N and 9°26.1'N [*Fornari et al.*, 1990; *Haymon et al.*, 1991; D. J. Fornari et al., unpublished data, 1993]. The images provided by the *Argo I* downward and forward looking video cameras, with a swath of approximately 13 m, resulted in more than 9 km^2 of visual coverage within the axial zone [*Haymon et al.*, 1991] and imaged approximately 80% of the ASC. South of 9°26'N, where no well-defined ASC exists, the density of visual coverage within the axial zone is ~40%. The density of visual and sonar imaging within the study area allowed the survey team to achieve its objectives: to determine the distribution of hydrothermal vents and deposits along the axial zone relative to fine-scale volcanic and tectonic features and to provide observations required for evaluating the potential of the area for the scientific drilling conducted on Ocean Drilling Program Leg 142 [*Batiza et al.*, 1992].

The character of the data requires some explanation as to what was actually observed and counted in the *Argo I* video and

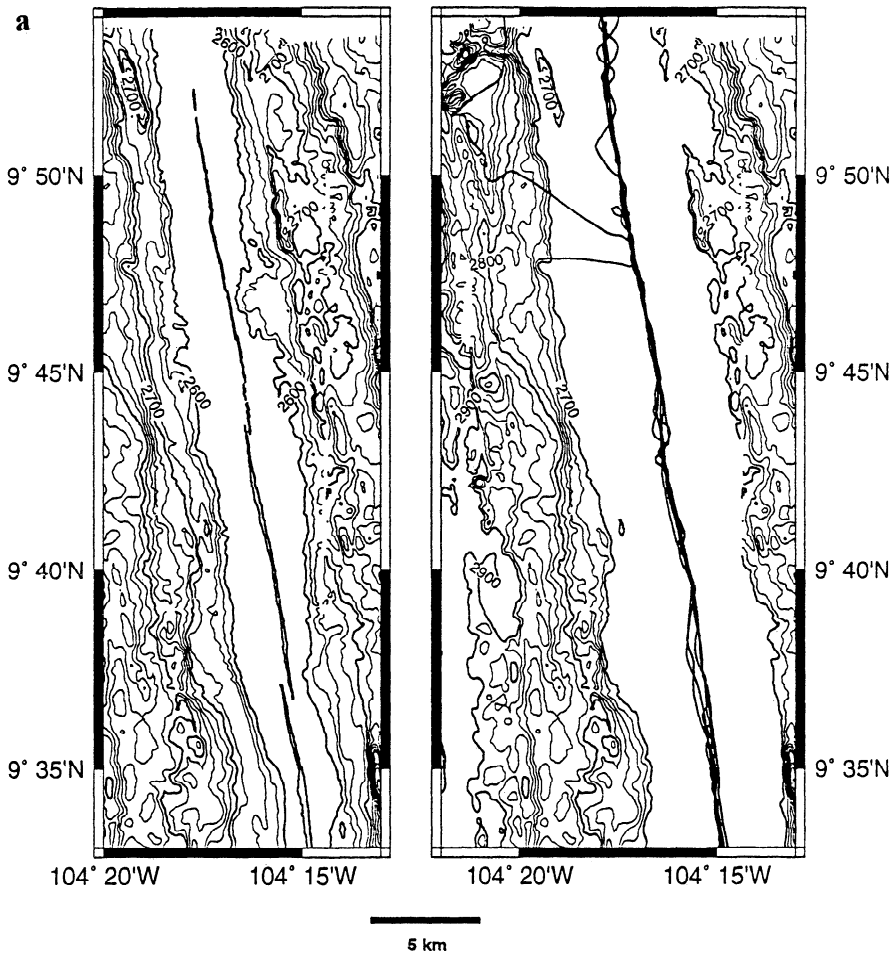

Figure 2. (a) Map of the East Pacific Rise from 9°33'N to 9°54'N showing (left panel) the approximate position of the outermost bounding walls of the ASC atop the ridge crest, as determined by *Argo I* sonar data, and (right panel) tracklines of the *Argo I* vehicle along the EPR axial zone. Bathymetric contours are from the Sea Beam data of *Wilcock et al.* [1993]. Contour interval is 20 m. (b) Position of the ASC bounding scarps (left) and *Argo I* tracklines (right) from 9°12'N to 9°33'N. Location of ODP Hole 864A shown by the stars. (c) Variation along the EPR ridge axis in the area of the axial zone visually imaged. Stars denote areas of special interest that were surveyed with greater trackline density and have correspondingly greater areal coverage.

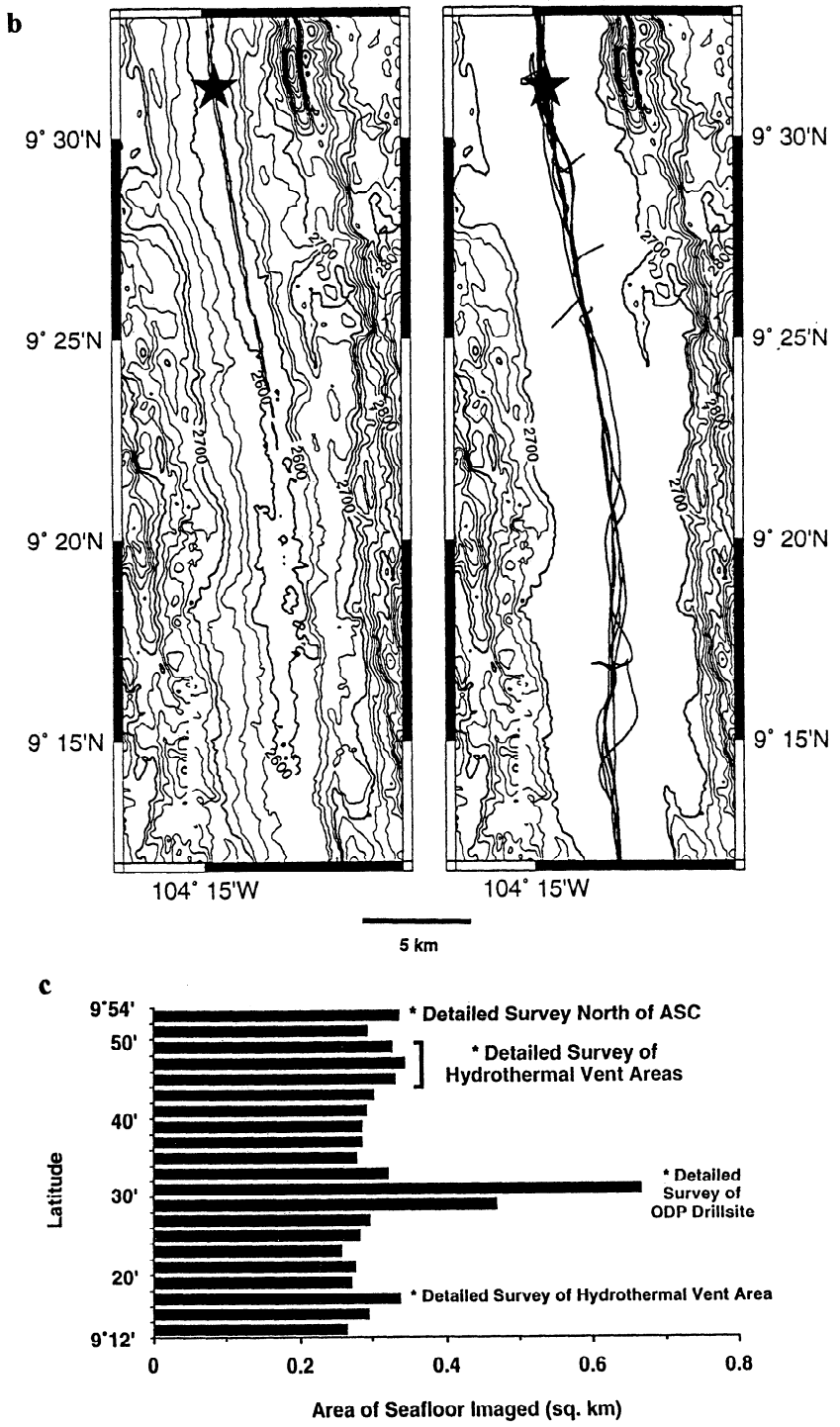

Figure 2. (continued)

sonar records. For this study, three types of fissures are classified: (1) cracks, breaks, or fractures in the crust that served as conduits for lava flows (eruptive fissures) (Figure 3a-3b); (2) cracks without lava flows issuing from them that apparently formed directly from lateral tensional stress (tectonic cracks or "gjar" as defined by *Thorarinsson et al.* [1959]) (Figure 3c); and (3) cracks forming from the shrinkage of cooling rock (thermal contraction cracks) (Figure 3d). In addition, long, narrow depressions or troughs formed by rivers of flowing lava (lava channels) were observed which were not classified as fissures (Figure 4). For features wide enough to be resolved on sonar records, it is relatively easy to distinguish lava channels (which are generally more sinuous and oblique to the ridge axis) from linear fissures (Figure 4). The *Argo I* sonar can detect features as small as ~5 to 15 m wide and ~50 to 100 m long [*Harris and Ballard*, 1986; *Edwards et al.*, 1990]. The small field of view for the video camera made it more difficult to judge the sinuosity of smaller lava channels that escaped detection by sonar, thus some of these features may be incorrectly classified as fissures. Wide troughs that took up almost the entire field of view of the video camera were always categorized as lava channels, not as fissures.

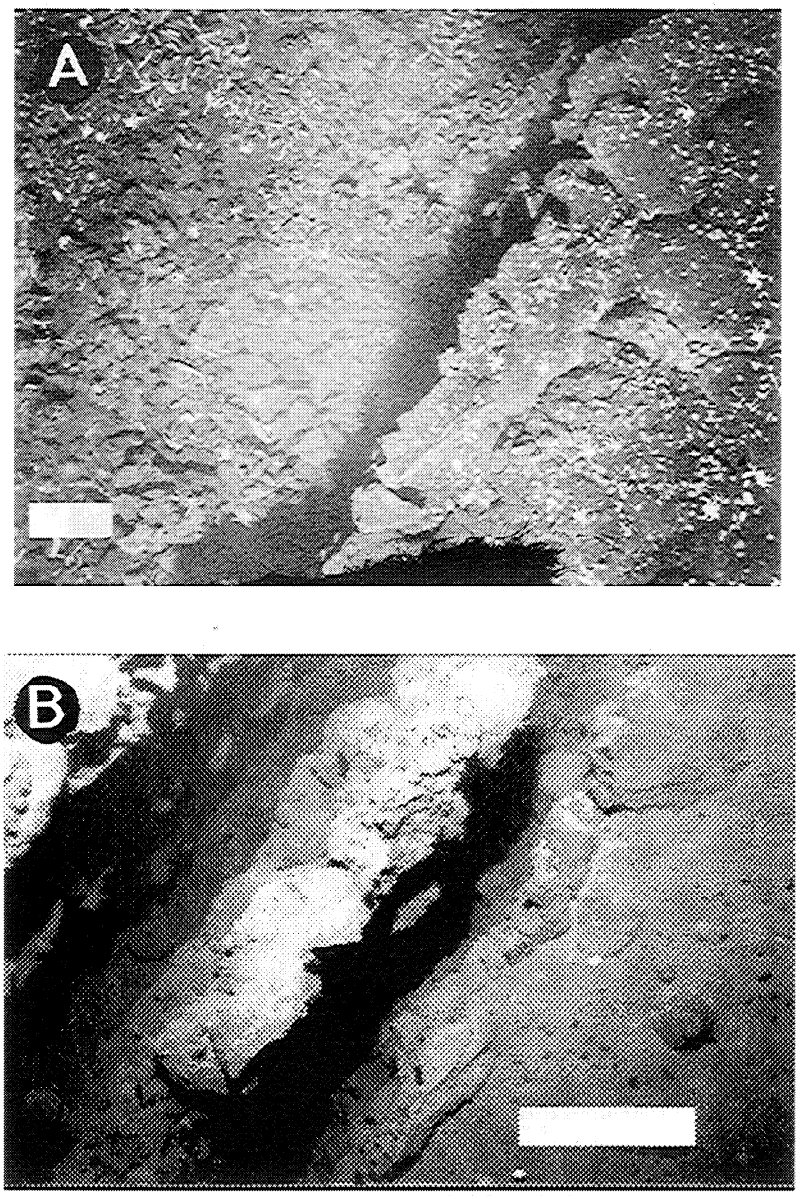

Figure 3. *Argo I* images of fissures and lava flows in the axial zone of the study area. Images are reprinted in black and white from the original color film for this publication. Scale bar in each image is 1 m, except for Figure 3b where the scale bar is ~5 m. See Figures 1 and 6 for image locations. (a) 35-mm photograph of a presumably eruptive fissure in relatively young lava. Plan view of hydrothermally active, 0.5-m-wide fissure in young (age 1) autobrecciated sheet flow along the axial zone of the East Pacific Rise, segment B, 9°49'N. Dense communities of mussels, clams, and *Galatheid* crabs seen in photo provide evidence of hydrothermal discharge. Depth ~2550 m, altitude ~6.0 m, heading ~10°. (b) Electronic still camera image of 5-m-wide (on left) and 2-m-wide (on right) fissures in older (age 2) sheet flows just outside the axial zone of the East Pacific Rise, segment B1, 9°50.0'N, 104°20.1'W. Depth ~2600 m, altitude ~6.0 m, heading ~340°. (c) 35-mm photograph of a presumably tectonic fissure in relatively old lava. Plan view of 0.3-m-wide fissure in relatively old (age 2) sheet flow along the axial zone of the East Pacific Rise, segment F, 9°22'N. Depth ~2574 m, altitude ~5.0 m, heading ~350°. (d) 35-mm photograph of narrow fissures, presumably due to tectonism or thermal contraction, in relatively old lava. Plan view of ~0.1-m-wide fissures in very old (age 3) sheet flow along the axial zone of the East Pacific Rise, segment E2, 9°31'N. Depth ~2580 m, altitude ~4.0 m, heading ~350°. (c) 35-mm photograph of a wide fissure in relatively old lava. Plan view of ~1-m-wide fissure in age 3 sheet flow along the axial zone of the East Pacific Rise, segment F, 9°25'N. Depth ~2590 m, altitude ~4.0 m, heading ~270°. (f) 35 mm photograph of relatively young lobate lava flows. Plan view of contact between very young (age 1) and older (age 2) lobate flows in the axial zone of the East Pacific Rise, segment F, 9°17.7'N. Depth ~2570 m, altitude ~4.0 m, heading ~350°.

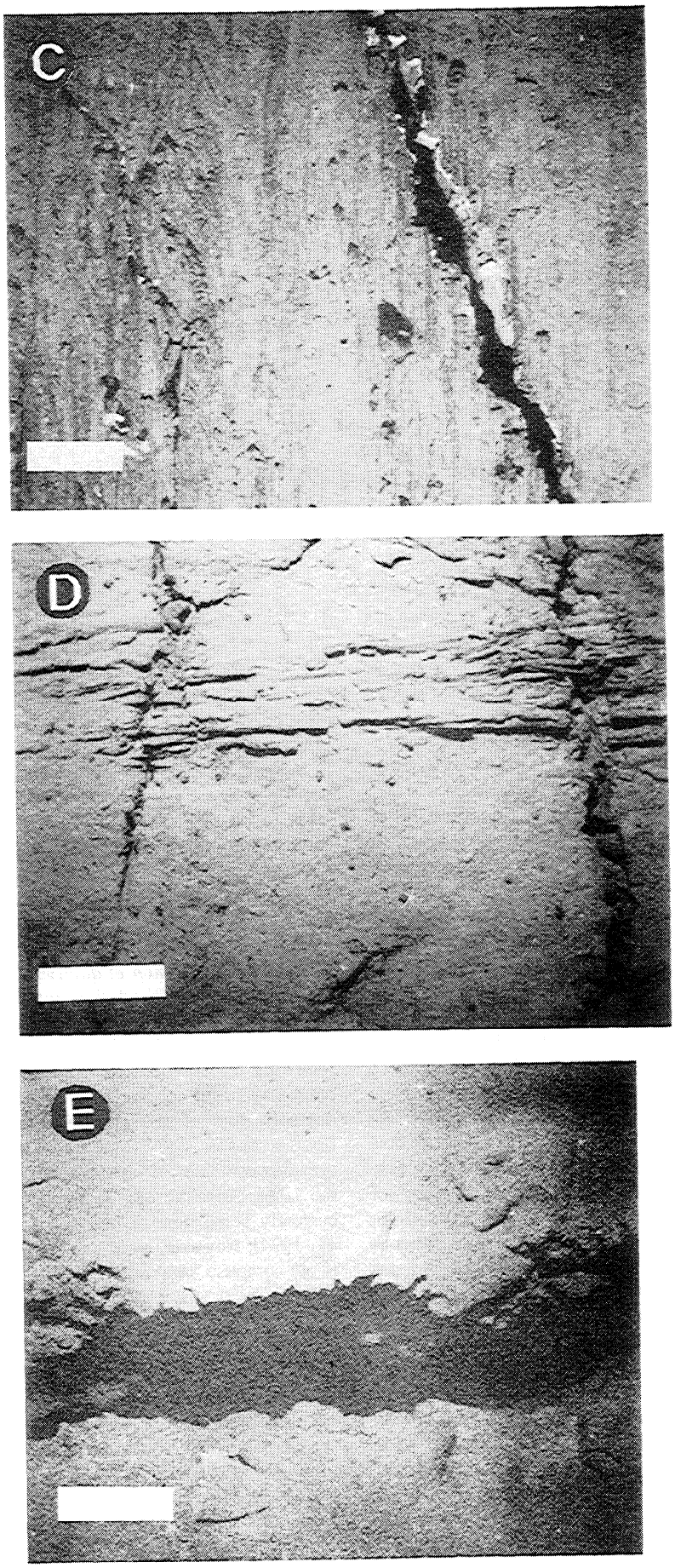

Figure 3. (continued)

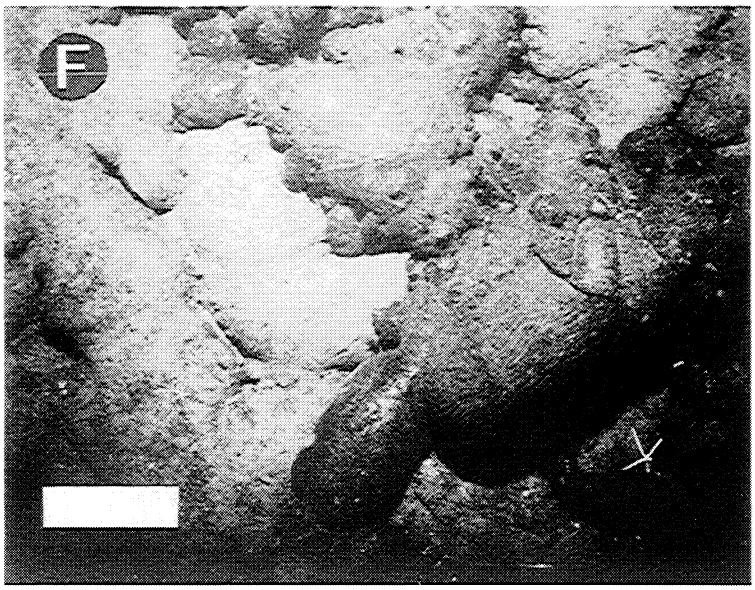

Figure 3. (continued)

Cracks created during the downslope movement of collapsing debris along the walls of the ASC (mass-wasting cracks) were also observed in the *Argo I* video and sonar records. In the *Argo I* videos near the rim of the ASC, these cracks could not really be distinguished from "gjar"-type cracks.

Relative age determinations of lava flows across spreading-center axes have been routinely made on the basis of sediment accumulation [e.g., *Ballard et al.*, 1981; *Lichtman et al.*, 1984; *Macdonald et al.*, 1988b; *Embley and Chadwick*, 1994]. Variations in volcanic surface morphology and relief, in hydrothermal sediment input, as well as in bottom currents capable of winnowing and redepositing fine sediment, all decrease the precision of relative age determinations based on sediment cover alone [*Lichtman et al.*, 1984; *Edwards and Zisk*, 1993]. However, careful study of *Argo I* photographs allows a first-order assignment of relative age based on the apparent thickness of small interpillow sediment ponds. Using previous visual lava-age criteria established by *Ballard et al.* [1981] and *Macdonald et al.* [1988b], six inferred relative age categories of ridge crest lava flows were distinguished by *Haymon et al.* [1991] in the *Argo I* video and electronic still camera images: "youngest" or age 1.0 lava flows (no sediment cover, highly vitreous luster on glassy flow surfaces); age 1.2 lava flows (light "peach fuzz" of sediment cover, vitreous luster); age 1.5 lava flows (light sediment cover within grooves and cracks in pillows, vitreous luster diminished, no sediment pockets); age 1.7 (no vitreous luster, very small sediment pockets (~2 cm across) on and between pillows; "intermediate" or age 2.0 flows (sediment pockets well developed between pillows and duller flow surfaces); and "oldest" or age 3 flows (sediment pockets deep enough to connect between pillows and dull, unreflective flow surfaces) (Figure 3). Using the *Haymon et al.* [1991] categories as a starting point, the geographic information system (GIS) was used to calculate average relative axial lava ages and to plot the map shown in Figure 5 (see the Appendix). To account for difficulties in consistently distinguishing between ages 1.2, 1.5, and 1.7 in the *Argo I* images, these lavas were grouped into a single category, "age 1-2." Since portions of the axial zone may contain lavas of different ages, the GIS was used to calculate the average bin and segment areas, which are used here and by *Haymon et al.* [1991]. In the Appendix a full description of the procedures for creating the map of relative lava age shown in Figure 5 is presented.

Haymon et al. [1991] estimated age 1 lava flows to be <50 years old, age 2 flows to be ~100-1000 years old, and age 3 lavas to be 1000-5000 years old. However, based on *Alvin* submersible observations made in the survey area during the AdVenture 1991 and 1992 dive programs [*Haymon et al.*, 1992, 1993], these estimates are now believed to be too old. The 1991 dive series occurred while the ridge axis between 9°45'N and 9°52'N was erupting "age 0" lava flows within and near the ASC [*Haymon et al.*, 1993]. Eleven months later, the 1992 dive series found that rapid initial accumulation of sediment on the age 0 flows had occurred due to a burst of hydrothermal and biological activity during and immediately following the eruption [*Haymon et al.*, 1992]. The non linear rate of sediment accumulation in the axial zone and the rapid devitrification of glassy lava crusts cause very young lava flows to appear significantly older than they really are; hence previous estimates of lava age may be an order of magnitude too large. Absolute age dating of lava flows in this area is currently being done [*Goldstein et al.*, 1993, 1994; *Rubin et al.*, 1994]. However, since calibration of an absolute age scale is not complete, only relative lava ages are used in this study.

Data Analysis

Volcanic, tectonic, hydrothermal, and biological phenomena observed on the black and white video were digitally logged in real time at sea and then merged with the vehicle navigation, which had already been median filtered for noise-spike removal and convolved with a Gaussian mask for smoothing. Simple format filters were then applied to convert the data for input to the *Arc/Info* GIS [*Environmental Systems Research Institute,* 1990]. This allowed the scientific party at sea to immediately archive four different types of seafloor

a

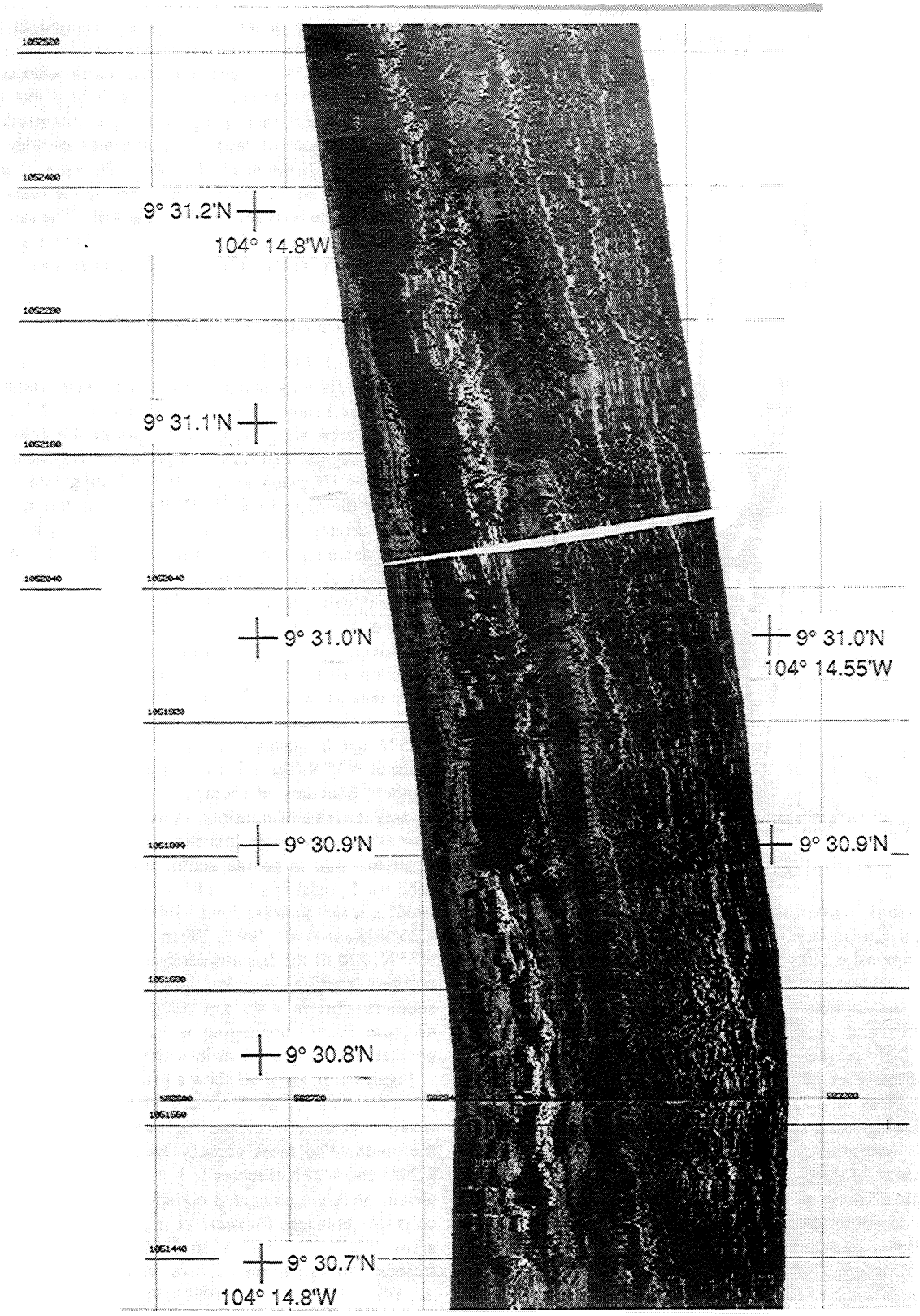

Figure 4. (a) *Argo I* 100-kHz side scan sonar image of EPR crest from 9°30.7' to 31.2'N showing a large lava channel and several wide fissures. White is high reflectivity, black is low reflectivity or shadows. The swath is approximately 300 m wide. (b) Interpretive map of side scan in Figure 4a.

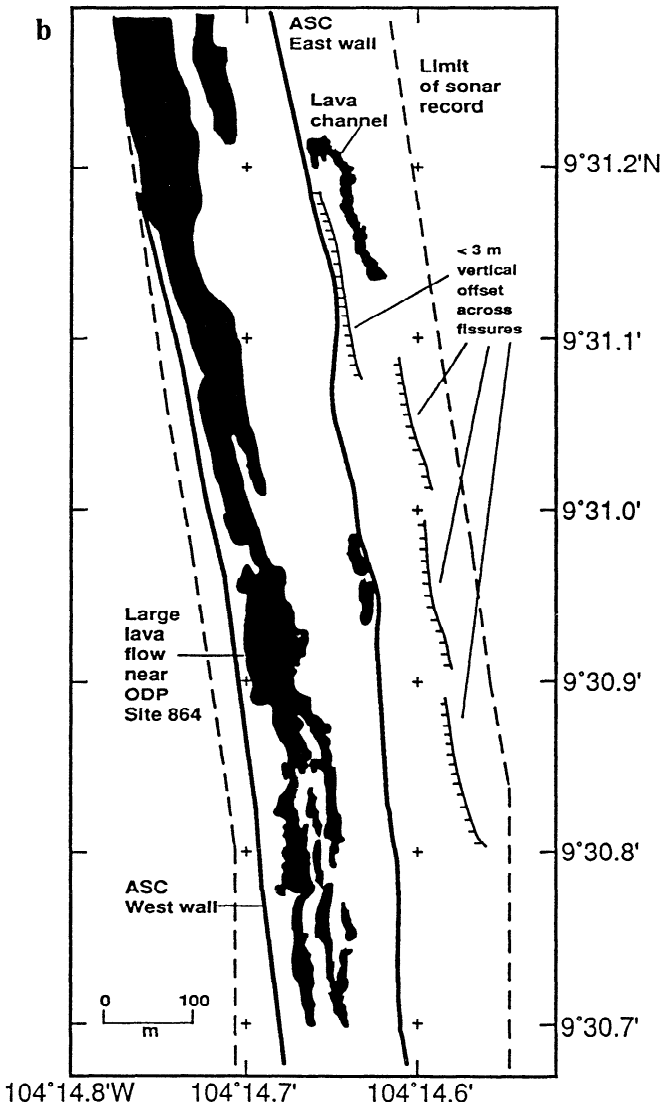

Figure 4. (continued)

observations (hydrothermal, volcanic, tectonic, and biological) in an organized and consistent manner and to obtain composite plots of the locations of vehicle tracklines and observed features. In general, the major importance of GIS lies in its ability to quickly establish correlations, proximities, and coincidences among data sets while keeping data in their correct geographic location [e.g., *Fox et al.*, 1988; *Maguire et al.*, 1991]. Spatial relationships between different types of data that might otherwise remain obscured while viewing just a single data set become apparent when the data are overlain. Such a capability was useful for the management of such a large and diverse data set of visual observations over an extensive geographic area. For this study, video observations of fissure crossings are represented in the GIS as zero-dimensional points in a Mercator projection (Figure 6). Information associated with each point includes the approximate width of the fissure. A full description of GIS data management methods is presented in the Appendix.

Histograms illustrating the distribution of features on a second-order scale were constructed in the following manner: The survey area was divided into 21 bins of 2 min latitude (3.7 km) by 4 min longitude (7.4 km). This bin size was chosen over smaller bin sizes because it was found to be the finest interval capable of capturing meaningful variation. This is in the realm of the "statistics of small numbers" in that the average number of fissures within a 2-minute bin is only 40. Binning the data at smaller intervals resulted in excessive "noise" (for example, the average number of fissures per 500-m bin was only 5). For analyses on a fourth-order scale (5-15 km along strike), the survey area was divided into unequally sized bins, each measuring 4 min of longitude by the latitudinal distance of each of the fourth-order ridge segments delineated by *Haymon et al.* [1991]. *Haymon et al.* [1991] picked fourth-order segment boundaries on the basis of devals or offsets of the bounding walls of the ASC. The same types of calculations were made to determine fissure density and average fissure width for each fourth-order segment.

Results at a Second-Order Scale

A total of 795 fissures (719 detected by video plus 76 additional fissures detected by sonar) were counted in the survey area. Features oriented outside of the 352 ± 10° trend of the ridge crest were excluded, as submersible observations in this area suggest that these are probably lava channels instead of fissures [*Haymon et al.*, 1993]. Taking into account the height of the *Argo I* vehicle off the bottom, the mean width of fissures detected by video is 2.5 m (minimum width is equal to 0.1 m, maximum width is equal to 8 m). Because of the spatial limitations of the video images, lengths were not determined for the population of fissures observed in the video. The mean width of the larger fissures detected by sonar is 9 m and the mean length is 151 m. Because the fissures detected by video make up 90% of the total population of fissures, only the video data set was used in the statistical analyses.

The survey area is divided into a younger portion north of 9°35'N (age 0-1 lavas on the ASC floor) and an older portion south of 9°35'N (age 1-2 lavas on the ASC floor); 9°35'N is the southern boundary of segment D. It is important not only as an area in terms of transition in axial lava age along strike but also as a morphologic transition in ASC width (widens from ~150 to ~400 m to the south, Figures 1 and 2) and as a subcrustal transition in width of the axial magma chamber (AMC), which narrows from ~700 to ~250 m to the south near 9°35'N [*Kent et al.*, 1993]. When the survey area is divided at 9°35'N, 210 of the fissures detected by video are found in the northern portion (~35 km long), compared to 509 in the southern portion (~43 km long). The mean width of the northern fissure population is 3.8 m, whereas the southern population averages 1.3 m in width.

Figures 1, 6, and 7 all show a pattern of fewer, wider fissures per unit area in the northern portion of the survey area trending to more abundant, narrower fissures per unit area in the south. The most densely fissured region lies between 9°20'N and 9°22'N (Figures 1, 3, 6, and 7) within an old (age 2) terrain of large, elongated collapse pits separated by narrow collapse remnants [*Fornari et al.*, 1990]. The least fissured areas, 9°20'-12'N and 9°46'-50'N, are regions where the freshest, youngest-looking lava flows are found [*Fornari et al.*, 1990; *Haymon et al.*, 1991] (Figures 1, 3, 6, and 7).

The 9°50'-54'N and 9°40'-44'N areas exhibit the widest fissuring (Figures 3 and 7). Both of these sites are adjacent to axial highs at 9°50'N and 9°40'N, respectively. The spatial correlation of wide fissures and axial highs is examined below in the Discussion section. The axial high centered at 9°50'N is the shallowest portion of the entire second-order ridge

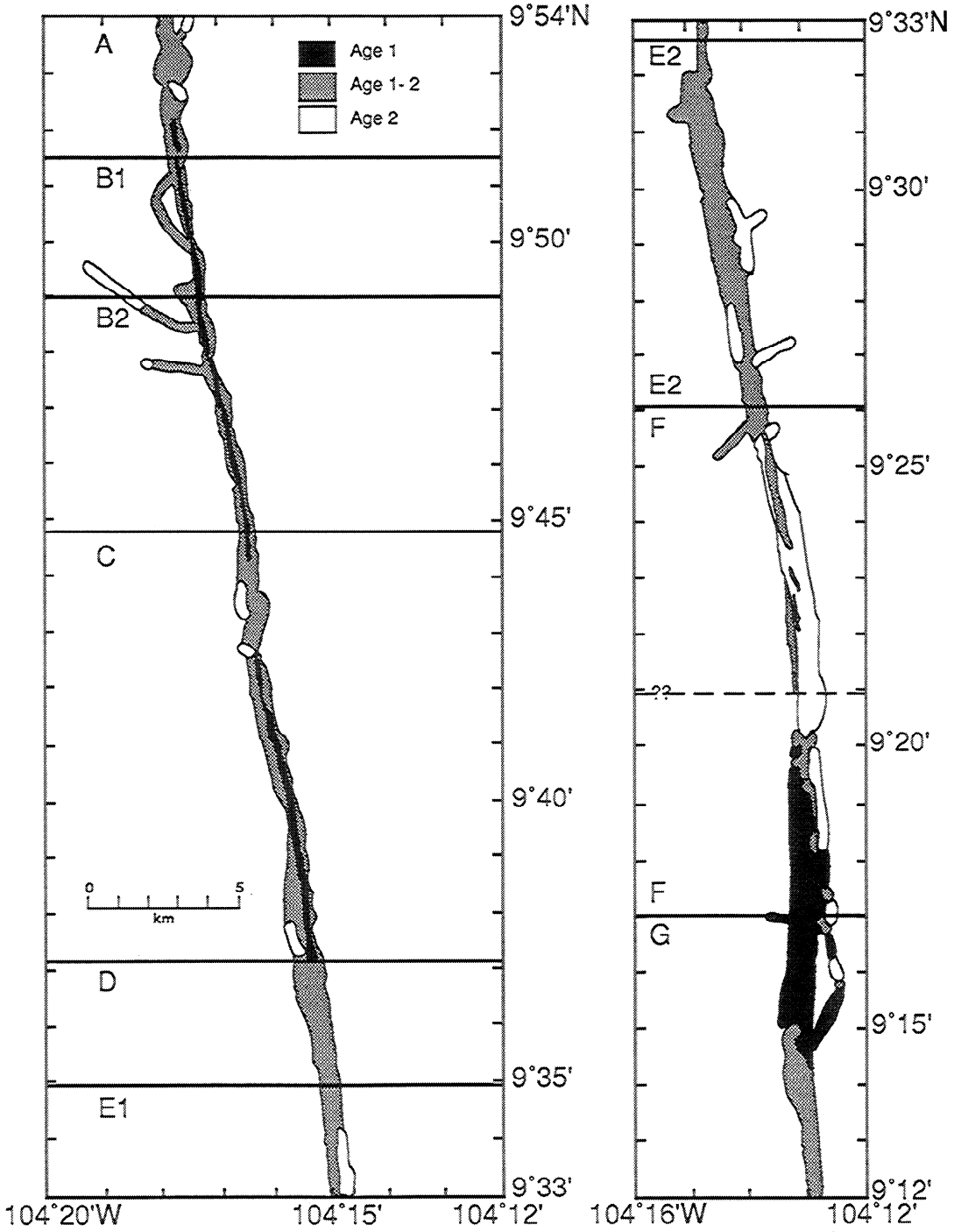

Figure 5. Map showing the approximate, along strike distribution of relative axial lava ages in the *Argo I* survey area. See the Appendix for discussion of the methods used to produce this map. Solid black lines mark the latitudes of fourth-order ridge segments, as determined by *Haymon et al.* [1991]. Map projection is Mercator.

segment between the Clipperton Transform and the OSC at 9°03'N. The Lamont Seamounts lie directly to the west of the axis at this latitude and are considered to result from excess magma in the mantle over a relatively wide zone west of the ridge axis [*Fornari et al.*, 1988]. Previous workers have speculated that the 9°50'N area is a primary injection point for melt that has segregated from the upper mantle [*Crane,* 1985; *Macdonald and Fox*, 1988]. It has been proposed that major melting events occur episodically in the upper mantle, due either to Raleigh-Taylor instabilities [*Whitehead et al.*, 1984; *Crane*, 1985; *Schouten et al.*, 1985] or to flow through a permeable medium [*Macdonald and Fox*, 1988]. Melt injection along the ridge axis at 9°50'N may have swelled shallow crustal and subcrustal magma reservoirs and provided the buoyancy required to support the axial high [*Crane,* 1985; *Macdonald and Fox*, 1988; *Wilson,* 1992]. Further evidence for magmatic injection in this region includes abundant high-temperature hydrothermal activity observed since 1989 and volcanic eruptions in 1991-1992 [*Haymon et al.*, 1993].

Density and widths of fissuring on a second-order scale

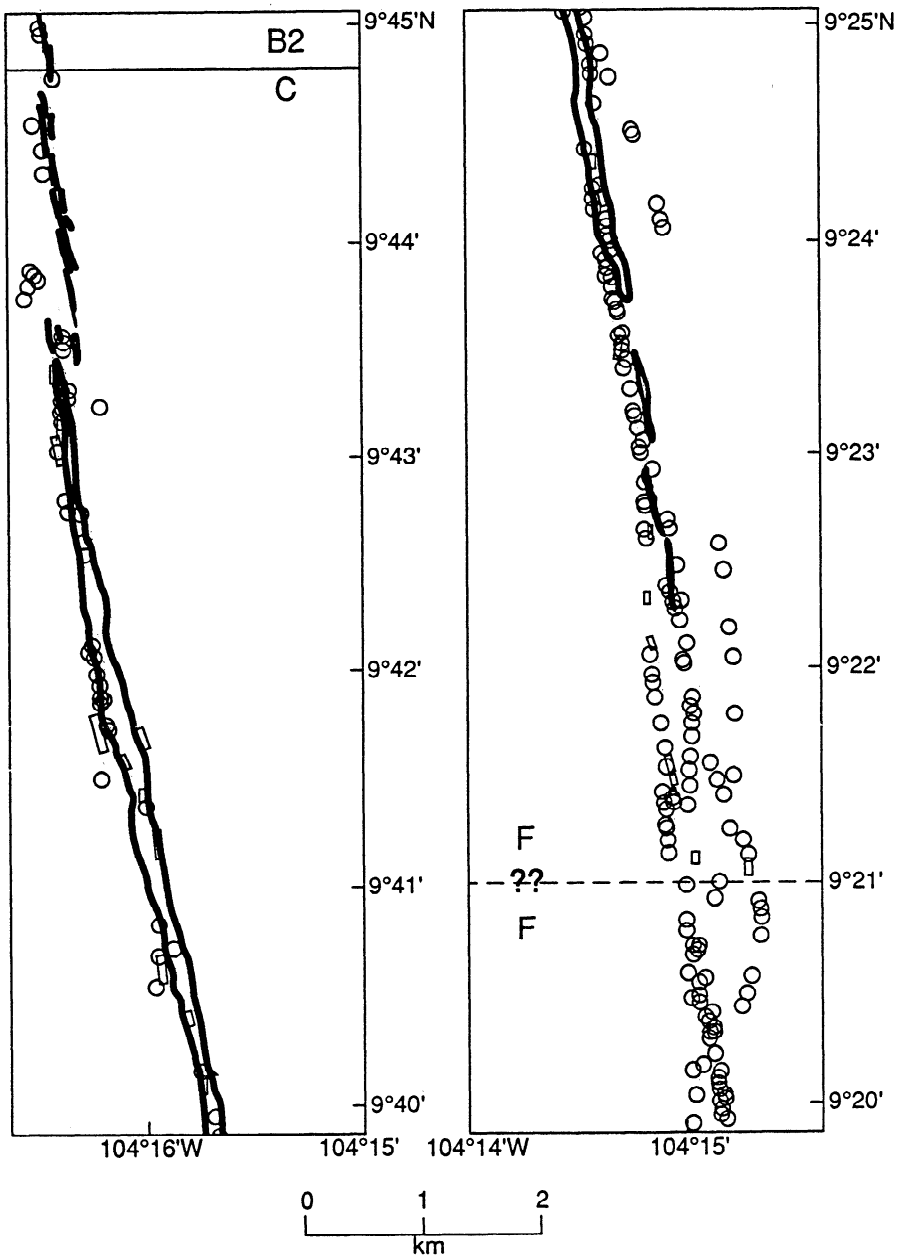

Figure 6. Map showing the distribution of fissures in the *Argo I* survey area from 9°40'-45'N to 9°20'-25'N, relative to the outer walls of the ASC as determined by *Argo I* sonar. The outermost walls of the ASC are denoted by solid black lines. Crossings of fissures as detected by *Argo I* video are shown by circles; fissures as detected by *Argo I* sonar are shown by rectangles. Overlapping circles do not represent crossings of the same fissure (see the Appendix). Map projection is Mercator.

correlate well with age distribution of axial lava flows. In general, lava ages and fissure densities increase as mean fissure widths decrease south of 9°35'N (Figures 3, 5, and 7). The widest fissures (ranging from 3 to 7 m in width, Figures 3 and 7) are found in the youngest lava flows (Figures 3 and 5) and dominate the fissure population in the northern portion of the survey area, whereas the older axial lavas south of 9°35'N contain many more relatively small fissures (ranging from 0.5 to 2 m in width). Two exceptions to the southward increase in lava age are the older (age 1.5) lavas on the northern side of the axial high at 9°50'N and the very fresh outcrops of young lavas between 9°12'N and 9°20'N (Figures 5 and 7). The correlation between lava age and fissure density holds for these two areas of anomalous age as well. The age 1.5 lava flows just to the north of the 9°50'N axial high are significantly more fissured than the age 1 flows just south of the axial high (Figures 1 and 7). The fresh, young pillowed and lobate flows of the 9°12'-20'N region, particularly from 9°14' to 16'N, are significantly unfissured in comparison to the southern survey area as a whole (Figure 7) (D. J. Fornari et al., unpublished data, 1993). These second-order-scale observations indicate that pre-existing cracks are covered and filled by new eruptions and that fissures are initially sparse and wide. As the ridge crest ages, it accumulates more but narrower cracks. Relatively few wide cracks are found among the many narrower ones in these older lavas (Figures 1,3e, and 5).

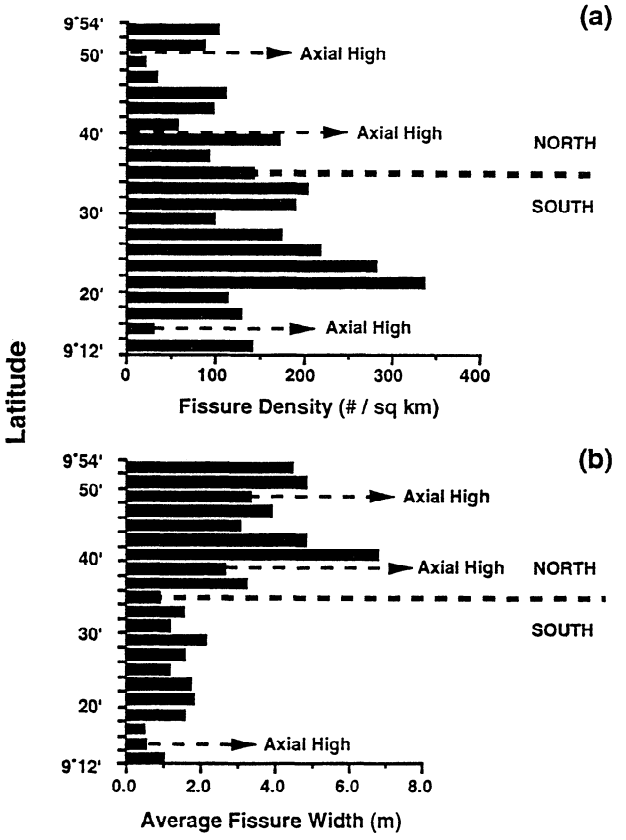

Figure 7. Variation along the ridge axis in (a) density of fissures per square kilometer of seafloor visually imaged and (b) average width of fissures (meters) in bins of 2' of latitude. The thick dashed lines separate both histograms into north and south regions (see text). The thin dashed lines point to the location of the 9°50'N topographic high along axis (the shallowest area on the EPR crest between the Clipperton Transform and the 9°03'N OSC) and the 9°40' and 9°15'N topographic highs.

Calculations of Cumulative Fissure Width

The summed widths of all fissures, including those detected by both video and sonar, were used to calculate the total amount of width added to the axial zone (500-m in width) by cracking (cumulative fissure width). In each latitudinal bin, the cumulative fissure width was normalized to the total width of the axial zone imaged by the *Argo I* camera. The resulting parameter, ΔL/L (where L is cross-sectional length after *Pockalny and Fox* [1989]), is plotted as a function of latitude in Figure 8. The most striking features of the ΔL/L profile in Figure 8 are the three prominent minima at approximately 9°49'N, 9°35'N, and 9°15'N. The 9°49'N and 9°15'N regions are areas where the youngest axial lavas occur, while the 9°35'N region is an older area (age 1.5, Figure 1). In the Discussion it is proposed that these minima mark the areas along the ridge axis that have most recently experienced mantle melt injection and resulting eruptions. These minima in ΔL/L are adjacent to maxima in the number of hydrothermal vents immediately to the north and south along strike (Figure 8). In contrast, the prominent maximum in ΔL/L at 9°21'N corresponding to the high density of fissuring in the region (Figure 7) is an area where virtually no hydrothermal activity has been observed [*Haymon et al.*, 1991].

Results at a Fourth-Order Scale

Each fourth-order segment is characterized by a mean fissure density that correlates with the mean axial lava age for that segment as well as with the abundance and type of hydrothermal vents. Within a fourth-order segment, however, fissure density varies along strike.

Figure 9a shows variations in the density of fissuring along strike, as a function of latitude, for most of the survey area. In most segments the density of fissuring reaches a maximum near the middle of a segment. This pattern is opposite to the pattern of cracking at a second-order scale, where cracking increases at segment ends [*Sempéré and Macdonald*, 1986; *Macdonald et al.*, 1991].

In general, fourth-order segments with younger axial lavas are less densely fissured and have a greater number of active hydrothermal vents than older segments (Figure 9a). For example, the density of fissuring is quite low at the northern and southern ends of segment B where the youngest axial lavas (age 1.0) and most abundant high-temperature hydrothermal vents occur based on *Argo I* observations [*Haymon et al.*, 1991] and where an eruption was documented in 1991 [*Haymon et al.*, 1993]. Moving southward to segment C, axial lavas are comparatively older (age 1.2, Figures 1 and 9b), and fissure density correspondingly increases (Figure 9a). Hydrothermal vents are not so abundant in comparison to the younger segment B. Continuing southward, the average age of axial lavas is greater in segment D (age 1.5), and the density of fissuring is correspondingly greater than the density in segment C (Figures 1 and 9). Hydrothermal activity is very minimal as established by *Argo I* data and *Alvin* diving [*Haymon et al.*, 1993]. Farther south along strike, segment E (age 1.7) contains some active vents as well as many inactive deposits [*Haymon et al.*, 1991], which suggests that it has been hydrothermally active for some time and is now in the waning stages of hydrothermal activity. Segment F, the oldest segment in the study area, is characterized by extensive fissuring in age 1.7 to 2.0 lavas and a general absence of hydrothermal activity (Figure 9a). Portions of this older, fissured terrain are covered by a field of extremely fresh, unfissured lobate lavas from 9°12' to 20'N. The young lava flows are associated with a black smoker at 9°16.8'N.

Discussion

Our near-bottom observations and statistical analyses have shown that the seafloor along the EPR crest between 9°12' and 54'N area generally gets older and more fissured along strike as the ridge axis deepens away from the 9°50'N axial high. In addition, less abundant, yet wider fissures in the northern portion of the survey area are associated with robust hydrothermal activity and topographic highs centered at 9°40'N and 9°50'N. These observations suggest that fissuring in the northern region may be governed in part by proximity to magmatic injection points from the upper mantle. On a second-order scale, the fine-scale structure of the 9° to 10°N ridge segment appears to be controlled largely by magmatic processes north of segment D, which has its southern terminus at ~9°35'N, and by tectonic processes south of segment D. The correlation of fissure density with axial lava age, at both second- and fourth-order scales, reveals the tendency of the crust to form more cracks with time, rather than to widen existing cracks formed early on. Superimposed on this temporal increase in crack density are spatially localized

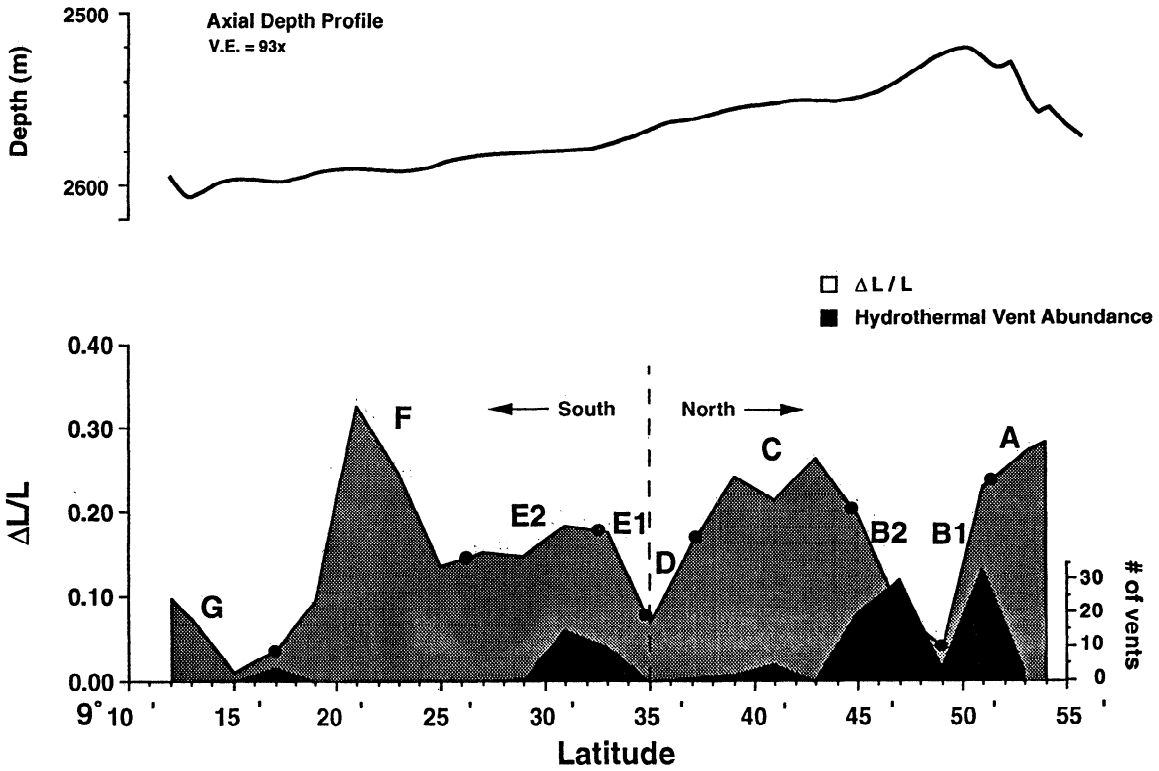

Figure 8. ΔL/L within axial zone surveyed by *Argo I* (shaded region) plotted along strike of the ridge axis as a function of latitude. ΔL/L is a dimensionless parameter representing the total amount of width added to the axial zone by cracking, divided by the total width of the axial zone imaged with the *Argo I* video camera. The calculations are made for bins of 2 minutes of latitude. Circles are placed at the latitudes of fourth-order ridge-axis discontinuities. A histogram of the number of vents actively discharging hydrothermal fluids per minute of latitude is overlain on the ΔL/L profile for comparison. Active vent count includes observed high-temperature vents (black, white, gray smokers, and smoke plumes) and low-temperature vents (milky or cloudy water; see Table 3 of *Haymon et al.* [1991]). Smoothed axial depth profile shown on top for comparison. Data are from the Sea Beam bathymetry of *Macdonald et al.* [1992]. Vertical exaggeration of axial depth profile is 93X.

effects on both fissure density and the distribution of fissure widths caused by inflation and eruption above possible sites of magma injection from the upper mantle.

Our calculations of along strike changes in cumulative fissure width (ΔL/L) have revealed three regions along the axial zone exhibiting minima in exposed cracking: along segment B at 9°49'-50'N; along segment D near 9°35'N; and along segment G near 9°15'N. These areas are interpreted as the most recent points of magmatic injection from the upper mantle along the EPR crest in the *Argo I* survey area, as described below.

The 9°50'N axial high on segment B appears to be a primary magmatic injection center, affecting the breadth and abundance of nearby fissures and the abundance and character of hydrothermal vents. Fissures widen markedly just to the north and south of this high, and fissure density significantly drops due to the filling and covering of fissures by very young lava flows just south of the 9°50'N axial high (Figure 7). The widths of the fissures indicate that their depths of crustal penetration along segment B are deep enough to reach Layer 2B (the sheeted dike complex) [*Christeson et al.*, 1992; *D.J. Wright et al.*, Breaking new ground: Estimates of crack depth along the axial zone of the East Pacific Rise (9°12'-54'N), submitted to *Earth and Planetary Science Letters*, 1994]. The wide, presumably deep cracks found along segment B are attributed to the propagation of dikes above and away from magma injection at the inflated 9°50'N axial high. These wide cracks are associated with a high density of hydrothermal venting (Figures 7 and 9). Narrower fissures in the older, southern portion of the *Argo I* survey area, where there is little hydrothermal activity, are calculated to be considerably shallower, i.e., confined to layer 2A (D. J. Wright et al., unpublished data, 1994). While from the *Argo I* images eruptive fissures cannot be unequivocally distinguished from those of purely tectonic origin, the occurrence of few but wide fissures in very young lavas and their spatial association with high-temperature vents lead to the proposition that these are deep fissure that tap melt, are primarily eruptive, and are loci for high-temperature hydrothermal discharge above dike intrusions. The narrower, presumably shallower fissures in relatively older lava flows are primarily tectonic and form within layer 2A in response to crustal extension and thermal contraction. Although all fissures provide pathways for seawater to enter the crust, which might potentially cool the hydrothermal and magmatic systems, it is suggested that most heat loss in the axial zone occurs early in the volcanic-hydrothermal-tectonic cycle along wide, deep, eruptive fissures that provide the most direct access to subseafloor dikes.

Recent *Alvin* observations confirm that many wide fissures

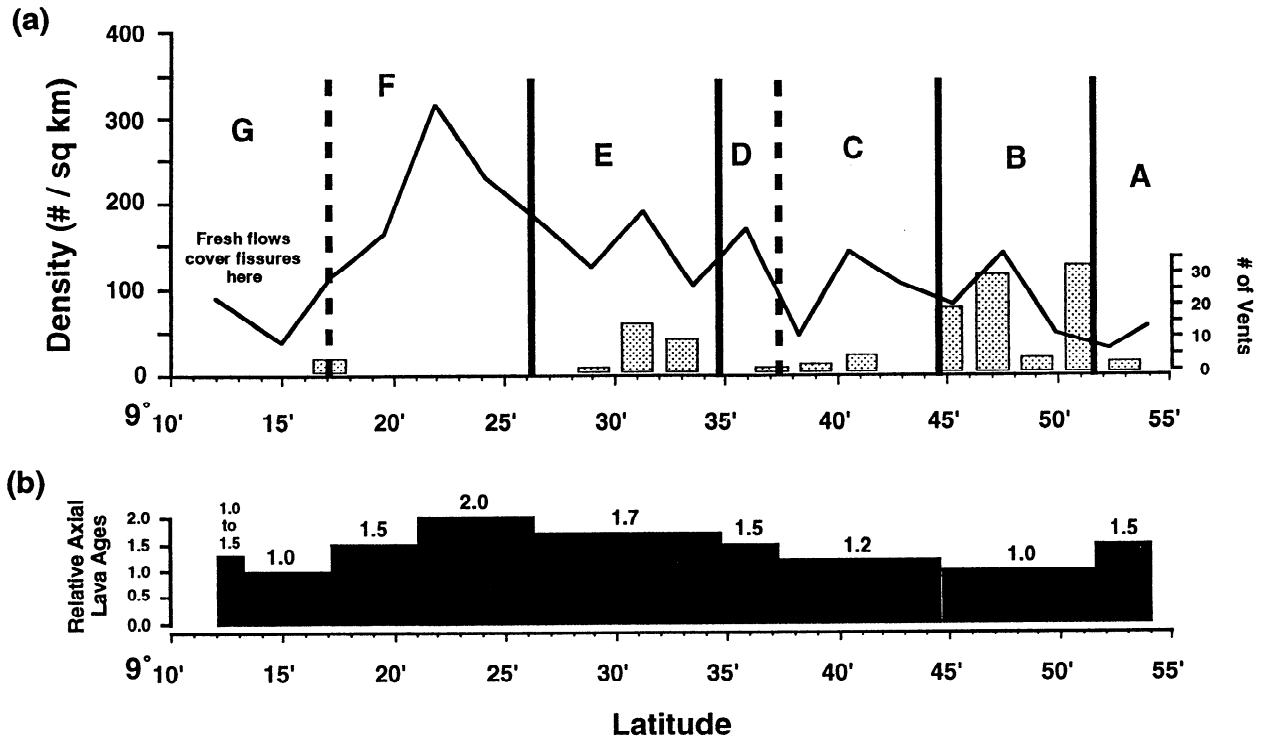

Figure 9. (a) Along strike variation in fissure density as a function of latitude for the *Argo I* survey area (bin size of 2' latitude). Dashed lines mark the latitude of fourth-order boundaries at discontinuities with a significant cross-strike offset and/or along strike overlap of the ridge axis. These discontinuities were not imaged as thoroughly as those with small offsets/overlap. Note the peaks in fissure density near the middle of most of the fourth-order segments. The number of vents actively discharging hydrothermal fluids per minute of latitude in 1989 is overlain for comparison. Active vent count includes high-temperature vents (black, white, gray smokers and smoke plumes) and low-temperature vents (milky or cloudy water; see Table 3 of *Haymon et al.* [1991]). (b) Along strike variation in relative axial lava age as a function of latitude for the *Argo I* survey area. See text for discussion of methods used to determine lava age. Lava age histogram is binned by age category as shown in Figure 1.

in the area appear to be eruptive in origin, and numerous high-temperature vents are localized along the margins of these wide fissures [*Haymon et al.*, 1993]. Similar observations have been made on portions of the Juan de Fuca Ridge [*U.S. Geological Survey*, 1986; *Embley and Chadwick*, 1994].

High-resolution seismic velocity profiles on the EPR axis at 9°30'N suggest that the top of the sheeted dikes resides at 150-200 meters below seafloor [*Christeson et al.*, 1992; *Harding et al.*, 1993; *Vera and Diebold*, 1994]. The depths of phase separation and quartz equilibration calculated for fluids collected from hydrothermal vents along the wide fissures of segment B during the 1991 eruption also extend to ~200 meters below seafloor [*Von Damm et al.*, 1991; *Haymon et al.*, 1993]. The seismic, geochemical, and geologic data together suggest that vent fluids boiled and equilibrated at the tops of the dikes feeding eruptive fissures along segment B in 1991 [*Von Damm et al.*, 1991; *Haymon et al.*, 1993].

Venting of hydrothermal fluids is more abundant along segment B than along any other fourth-order segment in the surveyed area. *Haymon et al.* [1991] proposed that hydrothermal flow in this area may consist of three-dimensional circulation of diluted lower-temperature fluids in the volcanic section above two-dimensional, ridge-parallel circulation of high-temperature fluids in the underlying sheeted dikes. In this conceptual model, high-temperature fluids within the sheeted dikes ascend and discharge onto the seafloor above zones of shallow dike intrusion, and recharging seawater enters the crust between dike intrusion zones [*Haymon et al.*, 1991, Figure 7]. For example, fluids discharging directly from fissures presumed to lie above shallow dikes along segment B may be recharged along segments A and C. Figure 10a illustrates the formation of hydrothermal vents along the edges of eruptive fissures above dikes. If newly erupted lavas fill and partially cover eruptive fissures, it is likely that as the fissures extend along strike above dikes propagating at depth, new discharge zones will develop in the fissure extensions above the dike tips (Figure 10b). This may explain the notable peaks in vent abundance observed on either side of the $\Delta L/L$ minima at 9°49'-50'N, 9°35'N, and 9°15'N (Figure 8), where possible eruptive fissures buried by relatively uncracked flows may be flanked by hydrothermally active fissure extensions. In summary, maxima in vent abundance may be found along fissures either just above the tops of intruding dikes (Figure 10a) or along fissures adjacent to eruptive volcanic vents (Figure 10b).

The $\Delta L/L$ minimum at 9°35'N just inside of segment D (Figure 8) is noteworthy because this region is not particularly close to an along-axis high (the closest being at 9°40'N) and appears to be moderately old (predominantly age 1.5 lavas); 9°35'N also marks an important transition along strike in volcanic and tectonic characteristics and subcrustal seismic characteristics of the ridge crest. For instance, lavas north of

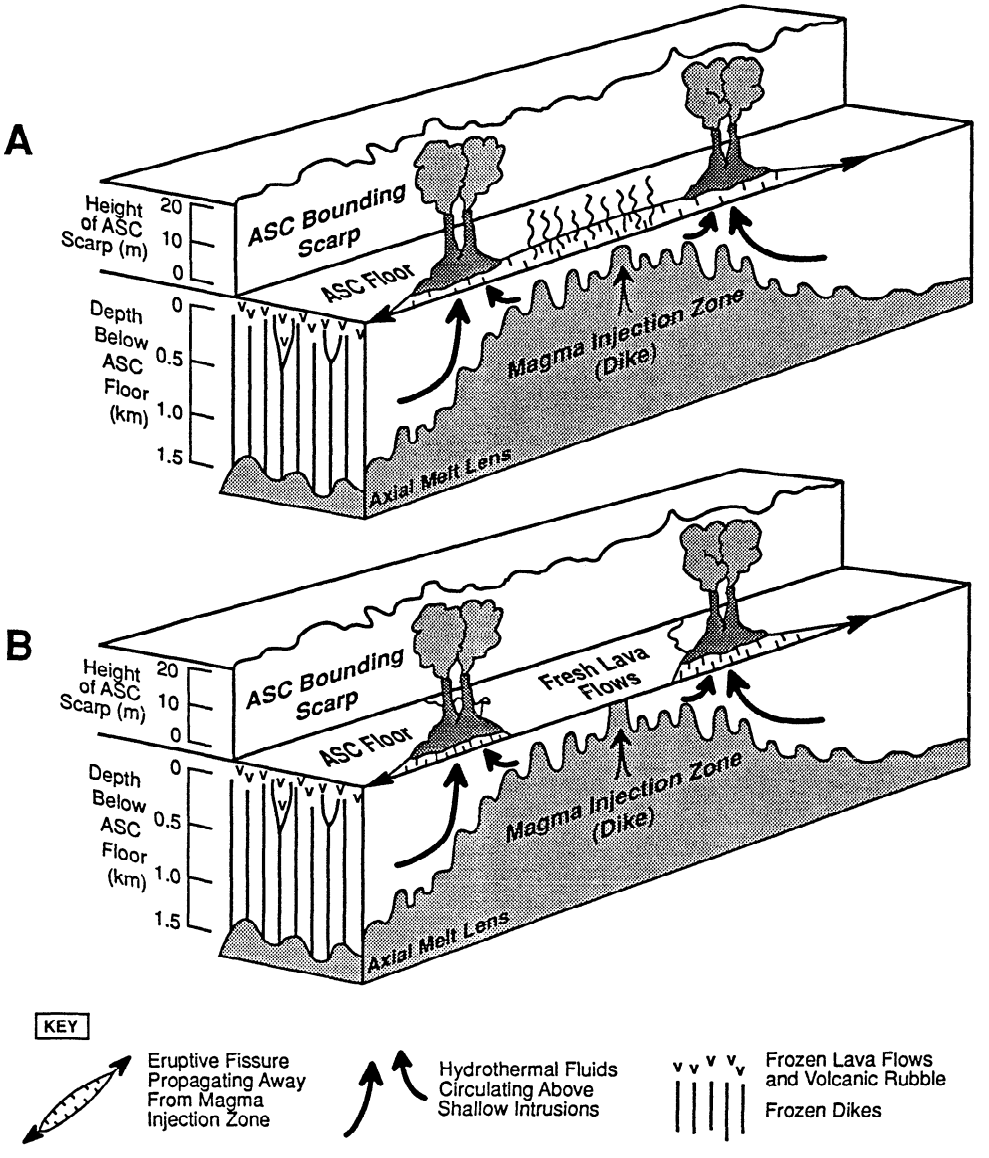

Figure 10. (a) Schematic block diagram illustrating the formation of hydrothermal vents along the edges of eruptive fissures, above dikes. Note the difference in vertical scale above and below the ASC floor. (b) If newly erupted lavas fill and partially cover eruptive fissures, it is likely that as the fissures extend along strike above dikes propagating at depth, new discharge zones will develop above the dike tips.

9°35'N are predominantly younger than lavas south of 9°35'N (Figure 5); the ASC widens southward at 9°35'N due to the coalescence of oblique segment D with segment E where they overlap (Figure 2); concurrently, the ASC at the northern end of segment D forms a miniature OSC with the ASC along segment C (9°37.1'N, Figure 2). The axis of the AMC reflector at 9°35'N is not centered beneath the ASC but is asymmetrically located ~1 km to the west [*Toomey et al.*, 1990; *Kent et al.*, 1993]. *Kent et al.* [1993] have also found that the width of the AMC here appears to pinch. The behavior of the AMC reflector in this region is consistent with the tomographic velocity perturbation imaged by *Toomey et al.* [1990] which suggests a reduction in temperature and perhaps melt volume across this discontinuity [*Kent et al.*, 1993]. Considering the whole of segment D, it is more densely fissured than the very young segment B, site of the ΔL/L minimum at 9°49'-50'N (Figure 7). A few extinct sulfide chimneys are present on segment D, and one active low-temperature vent lies at the southern tip of the segment. Segment D may have experienced a major magmatic episode within the past few hundred years, possibly related to a local reorientation of the axial zone. Hydrothermal activity is more robust just to the south of segment D, on segment E1 from ~9°31'-33'N (Figure 8), suggesting relatively recent dike injection along segment E1.

The ΔL/L minimum at 9°15'N (Figure 8) is explained by the presence of extremely fresh, newly erupted lavas which have covered or filled preexisting cracks. The exact location(s) of the recent eruptive vents is not certain but the ΔL/L minimum at 9°15'N is coincident with the 9°15'N axial high, which could be a mantle magmatic injection point. A fourfold increase in the width of the AMC reflector is also observed south of 9°17'N [*Kent et al.*, 1993]. As suggested by *Haymon et al.* [1991], the fresh lavas between 9°12'N and 9°21'N may

have emanated from the 9°15'N axial high and flowed south across the 9°17'N deval. More field observations are needed to establish the location of the volcanic vents feeding this lava field and to determine if there is any relationship between the recent volcanism and the dramatic along-strike changes in AMC width.

Fissure Density Variations at a Fourth-Order Versus a Second-Order Scale

Fissure density appears to increase near the centers of fourth-order segments and decrease near the tips of segments (Figure 9a). This is contrary to cracking patterns observed at a second-order scale, where crack density increases toward segment tips [*Sempéré and Macdonald*, 1986; *Macdonald et al.*, 1991]. The cracking pattern of second-order segments is associated with recent crustal extension or far-field tensile stress as the plates separate [*Sempéré and Macdonald*, 1986; *Macdonald et al.*, 1991]. Stresses result in a crack propagation force [*Macdonald et al.*, 1991] that promotes increased cracking at segment tips. This crack propagation force increases as the segment lengthens [*Macdonald et al.*, 1991]. The general paucity of fissures at the ends of fourth-order segments suggests that a different mechanism of fissuring is at work at this scale. The pattern of fissuring at this scale is driven by the propagation of dikes along strike away from small-scale, shallow, localized sites of melt injection from the magma lens and that fourth-order segment boundaries are thus null points between cracking fronts at the tips of advancing dikes (Figure 11).

Temporal Evolution of the Axial Zone and a Volcanic-Hydrothermal-Tectonic Cycle

Positive correlation of fissure density with relative ages of axial lavas reveals the tendency of the crust in the axial zone to accumulate more cracks with time rather than to widen existing cracks. This key observation implies that the occasional formation of wide, presumably deep cracks is intimately related to episodes of dike intrusion, eruption of new, uncracked flows, and hydrothermal venting. When intrusions and eruption cease, crustal cooling and extension continue to produce additional smaller, shallower cracks in the frozen volcanic carapace overlying the sheeted dikes. These cold, amagmatic cracks increase in number with time and normally are not sites of active hydrothermal discharge.

A second, highly important observation is that along strike variability in crustal fissuring and other fine-scale features of the seafloor correspond to the fourth-order morphotectonic segmentation of the ridge crest [*Haymon et al.*, 1991]. The tendency of fourth-order segment boundaries to coincide with along strike changes in the mean density of fissuring, in relative ages of axial lavas, and in hydrothermal vent abundances supports the premise of *Haymon et al.* [1991] that each 5 to 15-km segment is in its own phase of a volcanic-hydrothermal-tectonic cycle. Figures 12 and 13 summarize the data that constrain the cycle in space and time.

In the *Argo I* survey area the beginning phase of the cycle (Figure 13) is marked by vigorous magmatic and hydrothermal activity and the formation of wide fissures that are primarily eruptive in nature. These fissures appear to extend to depths below the base of layer 2A into the top of the sheeted dike complex (D. J. Wright et al., unpublished data, 1994). *Argo I* and *Alvin* submersible observations have documented the freshness of lavas and the abundance of young, high-temperature hydrothermal vents that are characteristic of this phase [*Haymon et al.*, 1991, 1993; *Embley et al.*, 1991, 1993; *Michard et al.*, 1984]. Segment B and parts of segment G are also representative of this phase. Heat loss from hydrothermal venting is at a maximum during this period.

The middle of the cycle is characterized by continued hydrothermal activity at older, well-established vents as well as the formation of more fissures due to the continued cooling and stretching of the volcanic carapace. This phase of the cycle may also include the occasional intrusion at depth of dikes which do not erupt new lava onto the seafloor but stimulate hydrothermal activity and increase discharge temperatures at existing vents. Segments A, C, D, E, and parts of segment G represent this phase (Figure 13).

The end of the cycle is marked by the cessation of magmatic and hydrothermal activity. The fissures in this phase of the cycle are distinct from earlier phases in that they are not associated with magmatism. These fissures are narrower and thus are inferred to be shallower than the depth to layer 2B (D. J. Wright et al., unpublished data, 1994). Cold seawater permeates the volcanic section and the hydrothermal and magmatic systems are temporarily shut down until the next cycle is triggered by dike intrusion. Segment F is representative of this phase, as it is a densely fissured, cooled segment, devoid of observed hydrothermal activity, with the largest amount of sediment accumulation (Figure 13).

Conclusions

1. On a second-order scale the seafloor along the EPR crest between 9°12' and 54'N surveyed by *Argo I* exhibits wider but less numerous fissures north of 9°35'N in relatively young lavas, trending to narrower, more ubiquitous fissures to the south in relatively old lavas. At this scale, the ridge segment appears to be controlled largely by magmatic processes along the northern portion of the surveyed area and tectonic processes in the south.

2. Contrary to the increased cracking toward segment tips observed at a second-order scale, fourth-order segments in the study area are, for the most part, more cracked in the middle rather than at the ends. This suggests that cracking on a fourth-order scale is driven by the injection and propagation of dikes rather than by far-field plate stresses.

3. Covariations in fissure density and axial lava ages reveal the tendency of the crust to form more cracks with time, rather than to widen existing cracks formed early on.

4. Superimposed on this accumulation of cracks are spatially localized, relatively recent eruptions that cover fissures and produce minima in $\Delta L/L$ (cumulative fissure width), near 9°49'-50'N, 9°35'N, and 9°15'N. In these regions, average fissure widths and depths may increase due to ridge crest inflation and dike propagation, resulting from recent magmatic replenishment of the AMC from upper mantle sources.

5. The tendency of young lavas to host sparse, wide fissures, which are spatially associated with abundant high-temperature vents, and the direct proportionality of crack depth to crack width (D. J. Wright et al., unpublished data, 1994). strongly suggest that wide fissures in relatively young lava flows are deep enough to tap melt; hence they are primarily eruptive. These fissures are loci for discharge of high-temperature hydrothermal vents above dikes. Narrower,

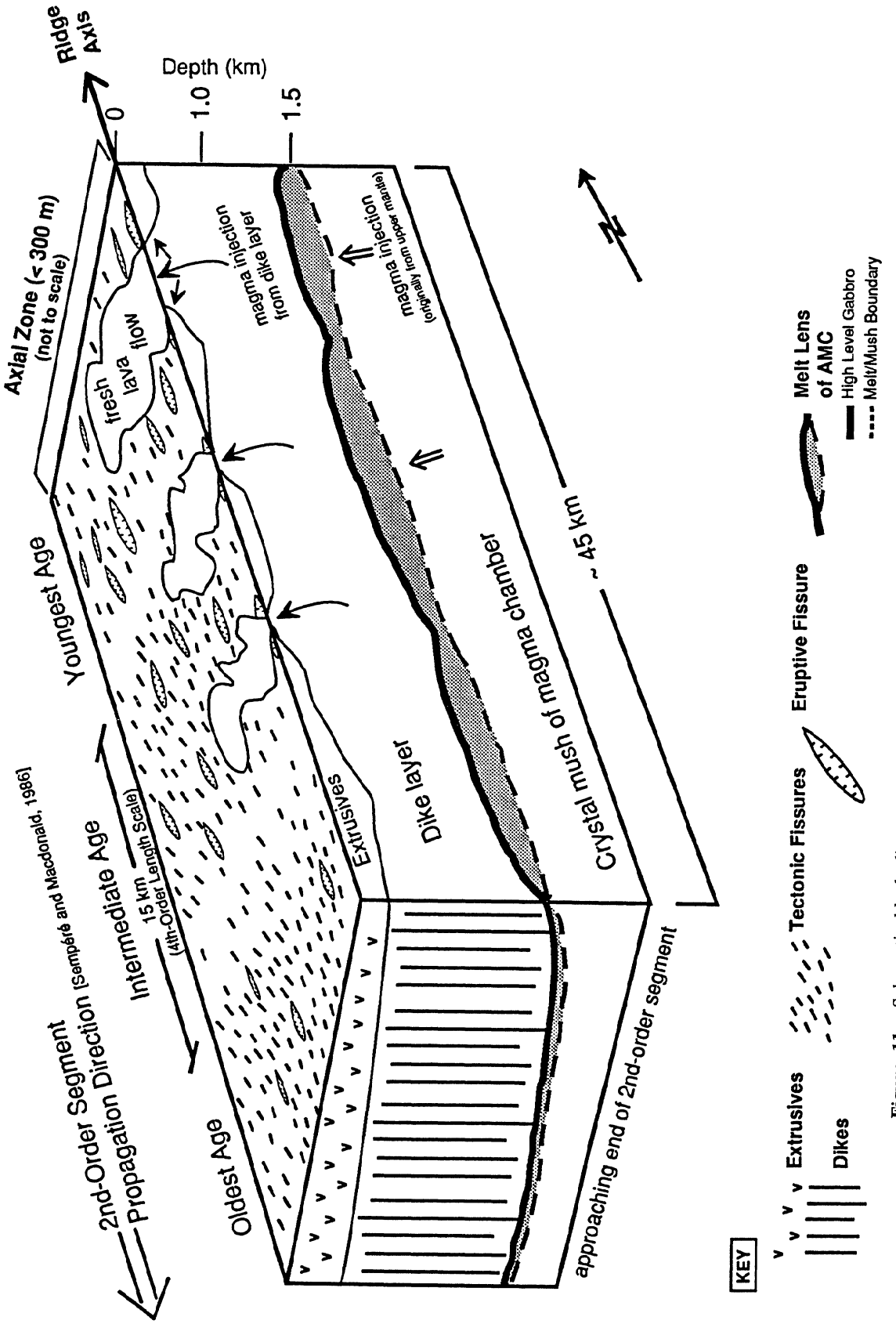

Figure 11. Schematic block diagram showing variations in the density and width of cracks observed along the EPR crest at 9°12'-54'N. This diagram distinguishes eruptive fissures from tectonic fissures and distinguishes fissure density distribution at a second-order scale from fissure density distribution at a fourth-order scale. Note that there are two levels at which magma injection occurs, as shown in the diagram. shallow injection from the dike layer and deep injection from the upper mantle.

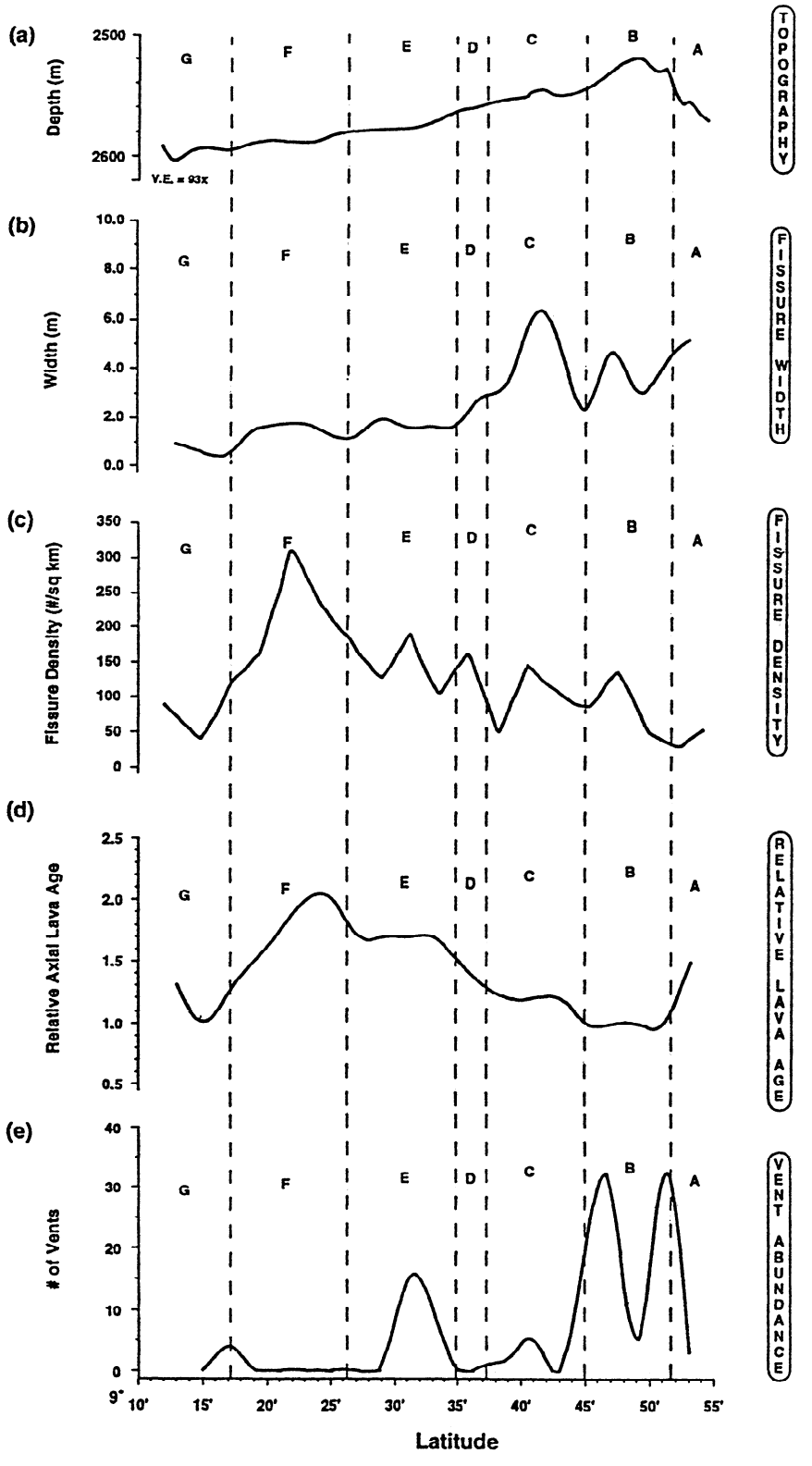

Figure 12. Stacked plots (versus latitude) of axial topography, average fissure width, fissure density, relative axial lava age, and hydrothermal vent abundance for the EPR crest, 9°12'-54'N. Vertical dashed lines mark the latitudes of fourth-order ridge axis discontinuities, as determined by *Haymon et al.* [1991]. Fourth-order segments are lettered A-F after *Haymon et al.* [1991]. (a) Seafloor topography from the Sea Beam bathymetry of *Macdonald et al.* [1992]. Vertical exaggeration is 93X. (b) Interpolated profiles of average and maximum crack width measured within bins of 2 min of latitude along strike. Error bars represent the standard errors (i.e., standard deviations of the mean) within each bin. (c) Along strike variation in crack density (i.e., the number of fissures per square kilometer of seafloor imaged with the *Argo I* video camera). (d) Along strike variation in relative axial lava age averaged within each ridge segment. Lava age criteria as in the work of *Haymon et al.* [1991]. (e) Along strike variation in the number of hydrothermal vents actively discharging hydrothermal fluids in 1989. Active vent count includes high-temperature vents (black, white, gray smokers, and smoke plumes) and low-temperature vents (milky or cloudy water).

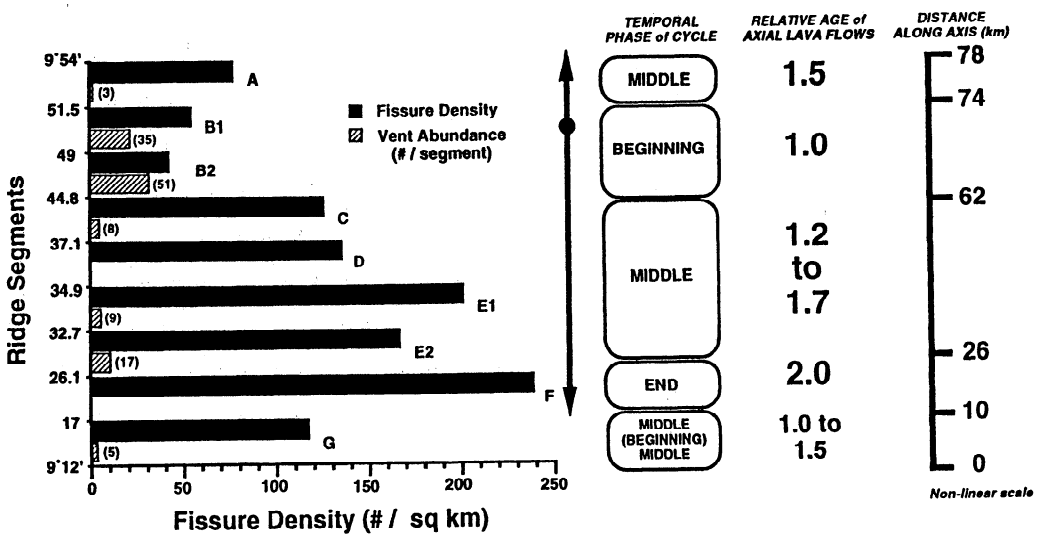

Figure 13. Illustration of the spatial and temporal constraints on a volcanic-hydrothermal-tectonic cycle in the *Argo I* survey area. The weighted density of fissures (per square kilometer of seafloor imaged) in each fourth-order ridge segment is represented by solid bars. The number of active high- and low-temperature vents per ridge segment is shown by the striped bars with the actual number in parentheses. The circle represents the 9°50'N axial high of the survey area, and the arrows extending above and below the circle represent both an increase in along strike depth and in axial lava age. Moving to the right, the next column identifies the temporal phase of a segment cycle and its approximate along strike extent. The phase of the cycle marked "BEGINNING" in parentheses at the bottom of the column refers to the fresh, unfissured flow spanning the boundary between segments F and G. Whether the source of the fresh flow is in segments G or F is uncertain; it is speculated that the source may be a local axial high, at ~9°15'N in segment G. The next column to the right identifies relative lava ages inferred according to the criteria of *Haymon et al.* [1991] and averaged within each ridge segment. The column on the far right scales the entire length of the study area, showing the along strike distance in kilometer.

shallower fissures in relatively older lava flows may be primarily tectonic features that form in response to crustal extension and thermal contraction. Because wide fissures form during the early, eruptive portion of the volcanic-hydrothermal-tectonic cycle and do not accumulate in the crust over time as narrower cracks do, only a few wide fissures are found among more numerous narrow fissures in older lavas. Even though all fissures provide pathways for seawater to enter the crust and cool the hydrothermal and magmatic systems, it is suggested that most heat loss occurs early in the volcanic-hydrothermal-tectonic cycle along the wide, deep, eruptive fissures.

6. Active hydrothermal vents are most abundant along segments that have experienced recent dike intrusion. At fast spreading centers, the distribution of these vents tends to be focused along primary eruptive fissures above the tops of dikes. Where eruptive fissures are filled and covered by lava flows, vents may be found at fissure ends above the leading tips of dikes propagating away from a central point of shallow, crustal magma injection.

On the fast-spreading EPR, fine-scale volcanic, tectonic, and hydrothermal characteristics of the axial zone strongly reflect the processes of ridge segmentation on both a second- and a fourth-order scale. The distribution of fine-scale features have spatially and temporally constrained the model of *Haymon et al.* [1991] in which the individual fourth-order segments are in different phases of a volcanic-hydrothermal-tectonic cycle that begins with cracking/diking and eruptive fissuring, followed by magmatic drainback, gravitational collapse, possible development of an ASC, and then cooling of the heat source, initiation of tectonic fissuring, and waning of hydrothermal and magmatic activity. At the end of the cycle, hydrothermal activity ceases, and cold tectonic cracking as well as mass wasting that widens the ASC, are the dominant processes modifying the axial zone.

Appendix: Geographic Information System (GIS) Data Management and Presentation

Video Data Editing

Postcruise editing of the video data involved a two-pronged effort: rendering the data (1) scientifically correct (i.e., ensuring that all features in the video footage were present in the GIS database and categorized properly and that all features in the GIS database were actually observed) and (2) spatially correct (i.e., ensuring that all feature attributes were linked to the correct navigational coordinates and that measurements of fissure widths were as accurate as possible). To accomplish this, the GIS database was double-checked against handwritten cruise logs and video footage. Where the widths of fissures seen in the video were not already specified, video footage was replayed, fissure widths were measured from the television monitor, and actual widths were calculated, taking into account the height of the vehicle from the seafloor (width of camera image is approximately 1.6 x vehicle altitude). Also considered were errors in vehicle navigation (the precision of the long-baseline, bottom-moored navigation was $\pm$5 m

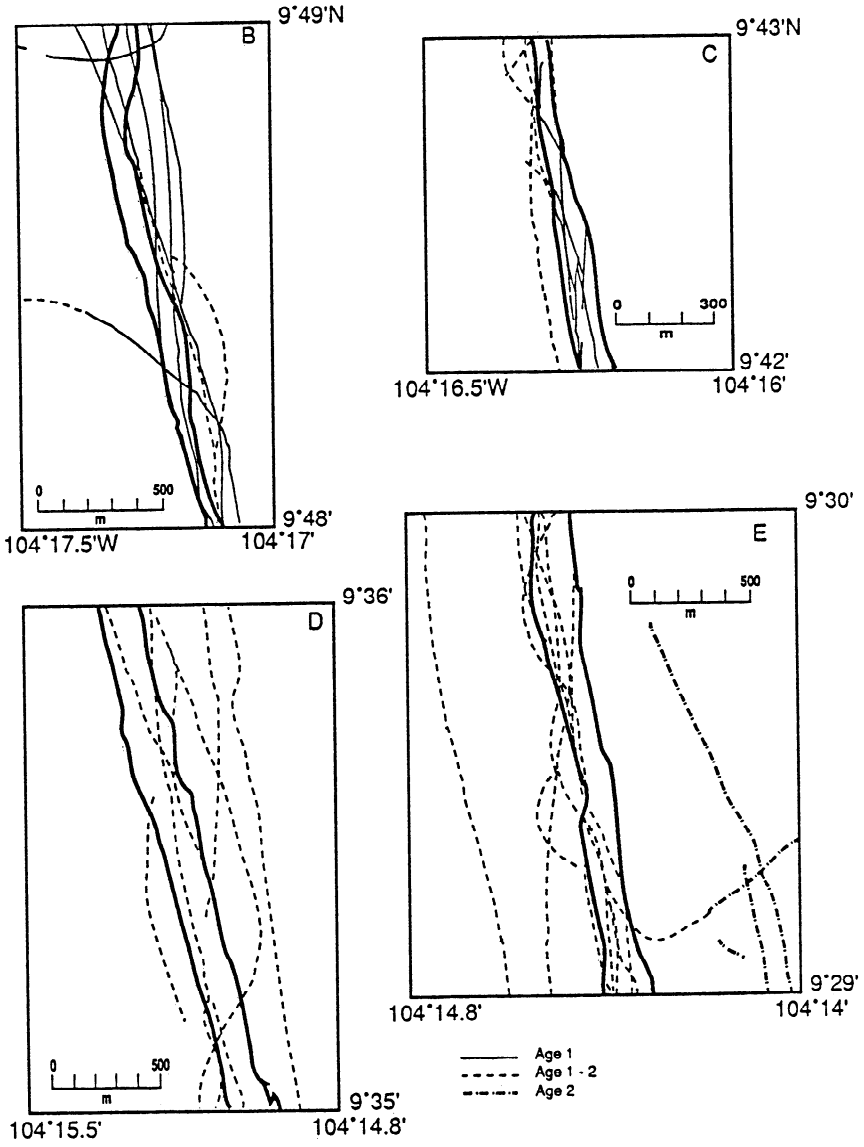

Figure 14. Geographic information system maps showing along strike observations of relative axial lava ages used to construct the lava age map of Figure 5 and to calculate mean ages within latitudinal bins and ridge segments. Thick solid lines denote the outermost walls of the ASC, other lines represent portions of *Argo I* tracklines along which video observations of lava ages were made. Note that age 1 lavas are largely found within the ASC, whereas older lavas are found mainly outside of the ASC. Lines representative of different ages that sometimes criss-cross illustrate the occasional ambiguity in visually estimating relative lava ages. Map projections are Mercator.

[*Haymon et al.*, 1991]) and errors introduced by the branching of fissures. To remedy this, the fissure data set was extracted from the GIS and then run through a FORTRAN decimation program. The program filtered the population of fissures by returning only one observation to the GIS if two or more fissures were within 10 m of each other in an east-west direction (which in reality accounted for only 5% of the entire population). This prevented the erroneous cataloging of two or more records for the same fissure within the database.

Sonar Data Editing

Edwards et al. [1990], *O'Brien et al.* [1990], and *Fornari et al.* [1990] provide detailed descriptions of the *Argo I* survey sonar-imaging geometry and postcruise acoustic processing techniques (including geometric and radiometric corrections). White areas in the sonar records depict strong acoustic returns from structures with slopes that face the sonar vehicle (similar to GLORIA; the opposite of SeaMARC II and HMR1; Figure 4). Shades of gray in the backscatter data represent returns of variable intensity from the hummocky volcanic terrain and can be used to determine the plan-view outline of lava flows with different surface textures. Black regions in the sonar data are in acoustic shadow or slopes away from the vehicle. Fissures that appear as thin black strips against a dark gray background indicate little or no vertical offset across the crack (Figure 4). Thin black strips that are fairly sinuous and show thin or muted acoustic returns on one or both edges are thought to be large lava channels (Figure 4). These were not included in the fissure data set. Sonar observations include all fissures greater than 5 m wide that could be seen in the 100-kHz records and are represented in the GIS as one-dimensional lines.

Relative Lava Age Editing and Overlay Analysis

Inferred relative lava ages were originally digitized into the GIS as nodes or endpoints, which represented the starting and ending of along-track video observations of flows of a particular age. The endpoints were converted to three classifications of lines, representing the along-track trace of an age 1, age 1 to age 2 (areas with mixtures of age 1.0, 1.2, 1.5, and 1.7 lavas), or age 2 flow (Figure 14). Age 3 lavas flows were distinguished on off-axis lines but were not observed within the axial zone. As a new way of visualizing the approximate distributions of axial lavas along the ridge crest, the lines were "buffered" into three categories of polygons using an arbitrary width of 300 m (the swath width of the *Argo I* sonar). Buffering is a form of proximity analysis where zones of a given distance are generated around selected geographic objects, i.e. points, lines, or polygons [*ESRI*, 1990]. The resulting buffer zones form polygons, or areas that are radially separated from each object by the specified buffer distance. The buffer width of 300 m was chosen for the most effective cartographic interpolation between the tracklines, allowing the GIS to fill in the space between tracklines where lava flow ages are known (Figure 5). Where tracklines were closely spaced, the buffers were clipped with GIS subroutines to fit the observations of lava flow age.

After all data sets were edited, topological overlay analysis [*ESRI*, 1990] was employed using the GIS capability of mathematically defining spatial relationships (e.g., distance, length, width, area, abundance) for all items in the data sets and then graphically displaying these data sets in any combination, either separately or uniformly. All "layers" or types of data were formatted and registered to the same spatial plane, allowing for exact geographic referencing among them. Geologic features and relationships were assessed within the different layers, and subsequent merging of these layers by enhanced computer graphics resulted in display of new spatial relationships. If desired, all related attribute files, tied to each layer of information by the GIS database, could be automatically joined.

Data Presentation

By the above methods it was possible to map where the *Argo I* video camera crossed a fissure, a high- or low-temperature hydrothermal vent (smoker, smoke, or cloudy water issuing from vent), a hydrothermal deposit (mound, chimney, edifice, hydrothermal sediment/staining), scattered biota or dense animal community, as well as fissure lineations, axial lava flow fronts, isolated fault scarps, the outer walls of the ASC, and the Sea Beam bathymetric contours of *Wilcock et al.* [1993] (e.g., Figures 5 and 6). By overlaying these features, spatial relationships among hydrothermal, volcanic, and tectonic features were quickly identifiable. Vehicle tracklines were also overlain on any combination of observations to note gaps or scarcity in data coverage or to test the validity of distributions, particularly in the extreme southern portion of the survey area (9°09' to 12'N) where density of trackline coverage is least.

The visual survey coverage calculations for Figure 2c were made by first generating 13-m-wide buffer zones around the *Argo I* tracklines (assuming an average vehicle height of 8 m; area of sonar coverage is approximately 23 times the area of visually imaged seafloor depicted here). The zones therefore represent the swaths of video coverage taken by *Argo I*. The survey area was then divided into 21 bins, each measuring 2 min of latitude. GIS was used to sum the areas of all swaths in each of the 21 bins for plotting of the histogram in Figure 2c. Off-axis tracklines extending farther than 1 km from the ridge axis were excluded from these calculations. The distribution of fissures outside the axial zone on the crestal plateau has not been well established and is beyond the scope of this study.

Acknowledgements. The *Argo* technical group at the Deep Submergence Laboratory of the Woods Hole Oceanographic Institution, the captain and crew of R/V *Thomas Washington*, and to all the participants of the Venture III expedition are gratefully acknowledged for their enthusiastic help and cooperation. Carol Brown and Tom O'Brien of the USGS-Woods Hole are thanked for assisting with computer facilities used to digitize lineations of the outer walls of the ASC and for converting the ASCII data files for direct input to the GIS; Dan Martin for helpful discussions on GIS procedures; Suzanne Carbotte, Ken Macdonald, Dan Scheirer, Russ Alexander, and Nell Beedle for fruitful discussions; and Angela Macias and Antoinette Padgett for their patience and skill in helping to drafting several of the figures. The critical reviews of Mike Coffin, Gail Christeson, Bob Embley, Ken Macdonald, and Dan Scheirer significantly improved the manuscript. This research was an Ocean Drilling Program site survey supported by National Science Foundation grants OCE-88-17587, OCE-89-11396 (both RMH), and OCE-88-17658 (DJF). DJW was also supported by the National Center for Geographic Information and Analysis at UCSB under Michael F. Goodchild (NSF grant SES-88-10917) and NASA grant NAGW-290-3 under Raymond C. Smith.

References

Ballard, R. D., J. Francheteau, T. Juteau, C. Ragnin, and W. Normark, East Pacific Rise at 21°N: The volcanic, tectonic, and hydrothermal processes of the central axis, *Earth Planet Sci. Lett., 55*, 1-10, 1981.

Batiza, R., M. Storms, and Leg 142 shipboard party, in *Leg 142 Preliminary Report*, Ocean Drilling Program, Texas A&M University, College Station, 1992.

Björnsson, A., Dynamics of crustal rifting in Iceland, *J. Geophys. Res., 90*, 10,151-10,162, 1985.

Chadwick, W. W., Jr., R. W. Embley, and C. G. Fox, Evidence for volcanic eruption on the southern Juan de Fuca Ridge between 1981 and 1987, *Nature, 350*, 416-418, 1991.

Christeson, G. L., G. M. Purdy, and G. J. Fryer, Structure of young upper crust at the East Pacific Rise near 9°30'N, *Geophys. Res. Lett., 19*, 1045-1048, 1992.

Crane, K., The spacing of rift axis highs: Dependence upon diapiric processes in the underlying asthenosphere?, *Earth Planet. Sci. Lett., 72*, 405-414, 1985.

Crane, K., Structural evolution of the East Pacific Rise axis from 13°10'N to 10°35'N: Interpretations from SeaMARC I data, *Tectonophysics, 136*, 65-124, 1987.

Crane, K., and R. D. Ballard, Volcanics and structure of the FAMOUS Narrowgate Rift: Evidence for cyclic evolution: AMAR 1, *J. Geophys. Res., 86*, 5112-5124, 1981.

Crane, K., F. Aikman III, and J.-P. Foucher, The distribution of geothermal fields along the East Pacific Rise from 13°10'N to 8°20'N: Implications for deep seated origins, *Mar. Geophys. Res., 9*, 211-236, 1988.

Detrick, R. S., P. Buhl, E. Vera, J. Mutter, J. Orcutt, J. Madsen, and T. Brocher, Multi-channel seismic imaging of a crustal magma chamber along the East Pacific Rise, *Nature, 326*, 35-41, 1987.

Eberhart, G. L., P. A. Rona, and J. Honnorez, Geologic controls of hydrothermal activity in the Mid-Atlantic Ridge rift valley: Tectonics and volcanics, *Mar. Geophys. Res., 10*, 233-259, 1988.

Edwards, M. H., and S. H. Zisk, The dimensions and ages of some submarine lava flows estimated using digital photographic data (abstract), *Eos Trans. AGU, 74*, 306, 1993.

Edwards, M. H., D. J. Fornari, T. A. O'Brien, and R. M. Haymon, High-

resolution Argo sonar data for the EPR crest 9°-10°N: Implications for ridge crest processes (abstract), *Eos Trans. AGU, 71,* 621, 1990.

Edwards, M. H., D. J. Fornari, A. Malinverno, W. B. F. Ryan, and J. Madsen, The regional tectonic fabric of the East Pacific Rise from 12°50'N to 15°10'N, *J. Geophys. Res., 96,* 7995-8018, 1991.

Embley, R. W., and W. W. Chadwick Jr., Volcanic and hydrothermal processes associated with a recent phase of seafloor spreading at the northern Cleft segment: Juan de Fuca Ridge, *J. Geophys. Res., 99,* 4741-4760, 1994.

Embley, R. W., I. R. Jonasson, M. R. Perfit, J. M. Franklin, M. A. Tivey, A. Malahoff, M. F. Smith, and T. J. G. Francis, Submersible investigations of an extinct hydrothermal system on the Galapagos Ridge: Sulfide mounds, stockwork zone, and differentiated lavas, *Can. Mineral., 26,* 517-539, 1988.

Embley, R. W., W. Chadwick, M. R. Perfit, and E. T. Baker, Geology of the northern Cleft segment, Juan de Fuca Ridge: Recent lava flows, sea-floor spreading, and the formation of megaplumes, *Geology, 19,* 771-775, 1991.

Embley, R. W., et al., Investigations of recent eruptive sites on the Juan de Fuca Ridge using the ROPOS: Revisits to the North Cleft 1980s eruption area and a fast response to a June/July eruption on the CoAxial segment (abstract), *Eos Trans. AGU, 74,* 561, 1993.

Environmental Systems Research Institute (ESRI), *Understanding GIS: The Arc/Info Method,* 514 pp., Redlands, California, 1990.

Fornari, D. J., M. R. Perfit, J. F. Allan, R. Batiza, R. Haymon, A. Barone, W. B. F. Ryan, T. Smith, T. Simkin, and M. A. Luckman, Geochemical and structural studies of the Lamont seamounts: Seamounts as indicators of mantle processes, *Earth Planet. Sci. Lett., 89,* 63-83, 1988.

Fornari, D. J., R. M. Haymon, M. H. Edwards, and K. C. Macdonald, Volcanic and tectonic characteristics of the East Pacific Rise crest 9°09'N to 9°54'N: Implications for fine-scale segmentation of the plate boundary (abstract), *Eos Trans. AGU, 71,* 625, 1990.

Fouquet, Y., A. Wafik, P. Cambon, C. Mevel, G. Meyer, and P. Gente, Tectonic setting and mineralogical and geochemical zonation in the Snake Pit sulfide deposit (Mid-Atlantic Ridge at 23°N), *Econ. Geol., 88,* 2018-2036, 1993.

Fox, C. G., K. M. Murphy, and R. W. Embley, Automated display and statistical analysis of interpreted deep-sea bottom photographs, *Mar. Geol., 78,* 199-216, 1988.

Gallo, D. G., et al., The Argo system: A reliable real-time, wide-area optical and acoustic seafloor mapping system (abstract), *Eos Trans. AGU, 71,* 622, 1990.

Gente, P., J. M Auzende, V. Renard, Y. Fouqet, and D. Bideau, Detailed geological mapping by submersible of the East Pacific Rise axial graben near 13°N, *Earth Planet. Sci. Lett., 78,* 224-236, 1986.

Goldstein, S. J., M. T. Murrell, and R. T. Williams, Pa^{231} and Th^{230} chronology of mid-ocean ridge basalts, *Earth Planet. Sci. Lett., 115,* 151-159, 1993.

Goldstein, S. J., M. R. Perfit, R. Batiza, D. J. Fornari, and M. T. Murrell, Off-axis volcanism at the East Pacific Rise detected by uranium-series dating of basalts, *Nature,* 367, 157-159, 1994.

Gudmundsson, A., and K. Bäckström, Structure and development of the Sveinagja Graben, Northeast Iceland, *Tectonophysics, 200,* 111-125, 1991.

Harding, A. J., G. M. Kent, and J. A. Orcutt, A multichannel seismic investigation of upper crustal structure at 9°N on the East Pacific Rise: Implications for crustal accretion, *J. Geophys. Res., 98,* 13,925-13,944, 1993.

Harris, S. E., and R. D. Ballard, Argo: Capabilities for deep ocean exploration, *Proc. Oceans '86, 1,* 6-9, 1986.

Haymon, R. M., D. J . Fornari, M. H. Edwards, S. Carbotte, D. Wright, and K. C. Macdonald, Hydrothermal vent distribution along the East Pacific Rise crest (9°09'-54'N) and its relationship to magmatic and tectonic processes on fast-spreading mid-ocean ridges, *Earth Planet. Sci. Lett., 104,* 513-534, 1991.

Haymon, R., et al., Dramatic short-term changes observed during March '92 dives to April '91 eruption site on the East Pacific Rise (EPR) crest, 9°45-52'N (abstract), *Eos Trans. AGU, 43,* 524, 1992.

Haymon, R. M., et al., Volcanic eruption of the mid-ocean ridge along the East Pacific Rise crest at 9°45-52'N, I, Direct submersible observations of seafloor phenomena associated with an eruption event in April, 1991, *Earth Planet. Sci. Lett., 119,* 85-101, 1993.

Kappel, E. S., and W. B. F. Ryan, Volcanic episodicity and a non-steady state rift valley along Northeast Pacific spreading centers: Evidence from Sea MARC I, *J. Geophys. Res., 91,* 13,925-13,940, 1986.

Kent, G. M., A. J. Harding, and J. A. Orcutt, Distribution of magma beneath the East Pacific Rise between the Clipperton Transform and the 9°17'N Deval from forward modeling of common depth point data, *J. Geophys. Res., 98,* 13,945-13,970, 1993.

Klitgord, K. D., and J. Mammerickx, Northern East Pacific Rise: Magnetic anomaly and bathymetric framework, *J. Geophys. Res., 87,* 6725-6750, 1982.

Langmuir, C. H., J. F. Bender, and R. Batiza, Petrological and tectonic segmentation of the East Pacific Rise, 5°30'N-14°30'N, *Nature, 322,* 422-429, 1986.

Lichtman, G. S., and J.-P. Eissen, Time and space constraints on the evolution of medium-rate spreading centers, *Geology, 11,* 592-595, 1983.

Lichtman, G. S., W. R. Normark, and F. N. Spiess, Photogeologic study of a segment of the East Pacific Rise axis near 21°N latitude, *Geol. Soc. Am. Bull., 95,* 743-752, 1984.

Lonsdale, P., Linear volcanoes along the Pacific-Cocos plate boundary, 9°N to the Galapagos triple junction, *Tectonophysics, 116,* 255-279, 1985.

Lonsdale, P., segmentation of the Pacific-Nazca spreading center, 1°N-20°S, *J. Geophys. Res., 94,* 12,197-12,225, 1989.

Luyendyk, B. P., and K. C. Macdonald, Physiography and structure of the inner floor of the Famous rift valley: Observations with a deeply towed instrument package, *Geol. Soc. Am. Bull., 88,* 648-663, 1977.

Macdonald, K. C., and P. J. Fox, The axial summit graben and cross-sectional shape of the East Pacific Rise as indicators of axial magma chambers and recent volcanic eruptions, *Earth Planet. Sci. Lett., 88,* 119-131, 1988.

Macdonald, K., J.-C. Sempéré, and P. J. Fox, East Pacific Rise from Siqueiros to Orozco Fracture Zones: Along strike continuity of axial neovolcanic zone and structure and evolution of overlapping spreading centers, *J. Geophys. Res., 89,* 6049-6069, 1984.

Macdonald, K. C., P. J. Fox, L. J. Perram, M. F. Eisen, R. M. Haymon, S. P. Miller, S. M. Carbotte, M.-H. Cormier, and A. N. Shor, A new view of the mid-ocean ridge from the behaviour of ridge-axis discontinuities, *Nature, 335,* 217-225, 1988a.

Macdonald, K. C., R. M. Haymon, S. P. Miller, J.-C. Sempéré, and P. J. Fox, Deep-Tow and Sea Beam studies of dueling propagating ridges on the East Pacific Rise near 20°40'S, *J. Geophys. Res., 93,* 2875-2898, 1988b.

Macdonald, K. C., D. S. Scheirer, and S. M. Carbotte, Mid-ocean ridges: discontinuities, segments and giant cracks, *Science, 253,* 986-994, 1991.

Maguire, D. J., M. F. Goodchild, and D. W. Rhind, *Geographical Information Systems: Principles and Applications,* 1096 pp., John Wiley, New York, 1991.

Michard, G., F. Albaréde, A. Michard, J.-F. Minster, J.-L. Charlou, and N. Tan, Chemistry of solutions from the 13°N East Pacific Rise hydrothermal site, *Earth Planet. Sci. Lett., 67,* 297-307, 1984.

Normark, W. R., Delineation of the main extrusion zone of the East Pacific Rise at Lat. 21°N, *Geology, 4,* 681-685, 1976.

O'Brien, T. A., M. H. Edwards, D. J. Fornari, and R. M. Haymon, Digital co-registration and comparisons between electronic still camera images and 100 kHz side-looking sonar data from the East Pacific Rise crest 9°-10°N (abstract), *Eos Trans. AGU, 71,* 621, 1990.

Pockalny, R. A., and P. J. Fox, Estimation of crustal extension within the plate boundary zone of slowly spreading mid-ocean ridges (abstract), *EosTrans. AGU, 70,* 1300, 1989.

Pollard D. D., P. T. Delaney, W. A. Duffield, E. T. Endo, and A. T. Okamura, Surface deformation in volcanic rift zones, *Tectonophysics, 94,* 541-584, 1983.

Rubin, A. M., and D. D. Pollard, Origins of blade-like dikes in volcanic

rift zones, in Volcanism in Hawaii, vol. 2, edited by R. W. Decker, T. L. Wright, and P. H. Stauffer, pp. 1449-1470, *U.S. Geol. Surv. Prof. Paper 1350,* Denver, Colo., 1987.

Rubin, A. M., and D. D. Pollard, Dike-induced faulting in rift zones of Iceland and Afar, *Geology, 16,* 413-417, 1988.

Rubin, K. H., J. D. Macdougall, and M. R. Perfit, Po^{210} - Pb^{210} dating of recent volcanic eruptions on the sea floor, *Nature, 368,* 841-844, 1994.

Schouten, H., K. D. Klitgord, and J. A. Whitehead, segmentation of mid-ocean ridges, *Nature, 317,* 225-229, 1985.

Sempéré, J.-C., and K. C. Macdonald, Deep-tow studies of the overlapping spreading centers at 9°03'N on the East Pacific Rise, *Tectonics, 5,* 881-900, 1986.

Sinton, J. M., and R. S. Detrick, Mid-ocean ridge magma chambers, *J. Geophys. Res., 97,* 197-216, 1992.

Thorarinsson, S., T. Einarrson, and G. Kjartansson, On the geology and geomorphology of Iceland, *Geogr. Ann., 11,* 135-169, 1959.

Toomey, D. R., G. M. Purdy, S. C. Solomon, and W. S. D. Wilcock, The three-dimensional seismic velocity structure of the East Pacific Rise near latitude 9°30'N, *Nature, 347,* 639-645, 1990.

U.S. Geological Survey Juan de Fuca Study Group, Submarine fissure eruptions and hydrothermal vents on the southern Juan de Fuca Ridge: Preliminary observations from the submersible *Alvin*, *Geology, 14,* 823-827, 1986.

Vera, E. E., and J. B. Diebold, Seismic imaging of oceanic layer 2A between 9°30'N and 10°N on the East Pacific Rise from two-ship wide-aperture profiles, *J. Geophys. Res., 99,* 3031-3042, 1994.

Von Damm, K. L., J. M. Grebmeier, and J. M. Edmond, Preliminary chemistry of hydrothermal vent fluids from 9-10°N East Pacific Rise (abstract), *Eos Trans. AGU, 72,* 480, 1991.

Whitehead, J. A., H. J. B. Dick, and H. Schouten, A mechanism for magmatic accretion under spreading centers, *Nature, 312,* 146-147, 1984.

Wilcock, W. S. D., D. R. Toomey, G. M. Purdy, and S. C. Solomon, The renavigation of Sea Beam bathymetric data between 9° and 10° N on the East Pacific Rise, *Mar. Geophys. Res., 15,* 1-12, 1993.

Wilson, D. S., Focused mantle upwelling beneath mid-ocean ridges: Evidence from seamount formation and isostatic compensation of topography, *Earth Planet. Sci. Lett., 113,* 41-55, 1992.

D. J. Fornari, Department of Geology and Geophysics, Woods Hole Oceanographic Institution, Woods Hole, MA 02543. (e-mail: fornari@tone.whoi.edu)

R. M. Haymon, Department of Geological Sciences and Marine Science Institute, University of California, Santa Barbara, CA 93106-9630. (e-mail: haymon@magic.geol.ucsb.edu)

D. J. Wright, NOAA-PMEL, Hatfield Marine Science Center, Newport, OR 97365. (e-mail: wright@new.pmel.noaa.gov)

(Received March 4, 1994; revised October 25, 1994;
accepted November 2, 1994.)